

## THE TEMPERATURE STRUCTURE OF 26 NEARBY CLUSTERS OBSERVED WITH ASCA. SIMILARITY OF TEMPERATURE PROFILES

MAXIM MARKEVITCH<sup>1,3</sup>, WILLIAM R. FORMAN<sup>1</sup>, CRAIG L. SARAZIN<sup>2</sup>, AND ALEXEY VIKHLININ<sup>1,3</sup>

*Submitted to ApJ, 1997 November 23*

### ABSTRACT

We present an analysis of ASCA spatially resolved spectroscopic data for a nearly complete sample of bright clusters with redshifts between 0.04 and 0.09. Together with several clusters from our previously published ASCA observations, this sample consists of 26 objects with  $T_e \gtrsim 4$  keV for which we obtained projected temperature profiles and, when possible, crude two-dimensional temperature maps. The clusters are A85, A119, A399, A401, A478, A754, A780, A1650, A1651, A1795, A2029, A2065, A2142, A2256, A2319, A2597, A3112, A3266, A3376, A3395, A3558, A3571, A3667, A4059, Cygnus A, and Triangulum Australis. All clusters, with the possible exception of a few with insufficiently accurate data, are found to be nonisothermal with spatial temperature variations by a factor of 1.3–2. ASCA temperature maps for many clusters reveal merger shocks. The most notable of these are A754, A2065, A3558, A3667, and Cygnus A; merging can also be inferred with lower confidence from the A85 and A119 temperature maps and from the A3395 and Triangulum Australis entropy maps. Including several mergers obvious from the images but for which our temperature maps are insufficiently accurate, about half of the sample shows signs of merging. Nearly all clusters show a significant radial temperature decline at large radii. For a typical 7 keV cluster, the observed temperature decline between 1 and 6 X-ray core radii (0.15 and  $0.9 h^{-1}$  Mpc) can be approximately quantified by a polytropic index of 1.2–1.3. Assuming such a polytropic temperature profile and hydrostatic equilibrium, the gravitating mass within 1 and within 6 core radii is approximately 1.35 and 0.7 times the isothermal  $\beta$ -model estimates, respectively.

Most interestingly, we find that all temperature profiles (excluding those for the most asymmetric clusters) appear remarkably similar when the temperature is plotted against radius in units of the estimated virial radius. We compare the composite temperature profile to a host of published hydrodynamic simulations. The observed profiles appear steeper than predictions of most Lagrangian simulations (Evrard, Metzler, & Navarro 1996; Eke, Navarro, & Frenk 1997). The predictions for  $\Omega = 1$  cosmological models are most discrepant, while models with low  $\Omega$  are closer to our data. We note, however, that at least one  $\Omega = 1$  Lagrangian simulation (Katz & White 1993) and the recent high-resolution Eulerian simulation (Bryan & Norman 1997) produced clusters with temperature profiles similar to or steeper than those observed. Our results thus provide a constraint for testing numerical simulations and discriminating among models of cluster formation.

*Subject headings:* Cosmology — galaxies: clusters: individual — intergalactic medium — X-rays: galaxies

### 1. INTRODUCTION

It has been twenty years since the realization that the extended X-ray emission from clusters (e.g., Kellogg et al. 1972) is thermal and arises from optically thin plasma filling the clusters (e.g., Mitchell et al. 1976). This plasma is in hydrostatic equilibrium in most clusters and delineates the distribution of the cluster gravitational potential. If one can measure the spatial distributions of the density and temperature of this plasma, it is possible to calculate the distribution of total cluster mass, including its dominant dark matter component (e.g., Bahcall & Sarazin 1977; Mathews 1978). Such measurements have cosmological implications. Most importantly, the observed high fraction of hot gas in the total cluster mass is a strong argument for a low value of the cosmological density parameter  $\Omega$  (e.g., White et al. 1993). The spatial distribution of the cluster plasma temperature is interesting in itself, because it is an indicator of the cluster dynamical state. Hydrodynamic simulations show that clusters which recently formed via mergers of smaller subunits should have a complex temperature structure which becomes more regular with time (e.g., Schindler & Müller 1993; Roettiger, Burns, & Loken 1993). Determination

of the dynamical state of present-day clusters can, in principle, constrain cosmological models (e.g., Richstone, Loeb, & Turner 1992), because rich clusters should be dynamically older in an open universe than in a high-density universe (e.g., White & Rees 1978). Although recent simulations (e.g., Thomas et al. 1997) suggest that the degree of irregularity of the cluster images is not as strongly dependent on  $\Omega$  as it was thought, temperature maps contain additional information on the cluster dynamics that may enable more sensitive tests. The spatial distribution of cluster temperatures also may provide clues on the significance of nongravitational sources of gas thermal energy, such as supernovae-driven galactic winds (e.g., Metzler & Evrard 1997).

The most promising quantitative approach to these interesting problems is to compare the observed cluster temperature and density structure with predictions of cosmological hydrodynamic simulations. Presently, independent simulation techniques seem to converge on the same qualitative results for cluster dark matter and gas distributions within the framework of their assumed physical models (e.g., Frenk et al. 1998), although their resolution is still insufficient to model the fine de-

<sup>1</sup>Harvard-Smithsonian Center for Astrophysics, 60 Garden St., Cambridge, MA 02138; maxim, wrf, alexey @head-cfa.harvard.edu

<sup>2</sup>Department of Astronomy, University of Virginia, Charlottesville, VA 22903; cls7i@virginia.edu

<sup>3</sup>Also Space Research Institute, Russian Academy of Sciences

tails of the gas density distribution. In some sense, the opposite holds for present-day observations — while the X-ray imaging instruments such as *Einstein* and *ROSAT* have obtained high-resolution gas density maps for a large number of clusters, until recently, detailed spatially resolved temperature data were unavailable. The early X-ray spectroscopic instruments lacked imaging capability, while imaging instruments had limited spectral resolution or bandwidth. Coarse spatial temperature distributions were obtained only for the nearest clusters such as Coma, Perseus, and Virgo with *EXOSAT* (Hughes, Gorenstein, & Fabricant 1988), *Spacelab-2* (Eyles et al. 1991; Watt et al. 1992), and *Ginga* (Koyama, Takano, & Tawara 1991). The *ROSAT* PSPC was the first instrument to combine good spatial and adequate spectral resolution for energies below 2 keV. It obtained temperature distributions for several galaxy groups and cool clusters (e.g., Ponman & Bertram 1993; David, Jones, & Forman 1995). The *ROSAT* temperature maps for several hot clusters were published as well (e.g., Briel & Henry 1994, 1996; Henry & Briel 1995, 1996), but see Markevitch & Vikhlinin (1997a, hereafter MV97a) for a more realistic estimate of their uncertainties.

The *ASCA* X-ray observatory (Tanaka, Inoue, & Holt 1994) is capable of measuring the temperature distributions in nearby clusters. The *ASCA* energy band (0.5–11 keV) is well-suited for clusters, and the 3' half-power diameter angular resolution is adequate. Although analysis of the *ASCA* data is complicated by the mirror effects such as the energy dependence of the point spread function (Takahashi et al. 1995) and sometimes stray light (Ishisaki 1996), there are published results on cluster temperature structure that take these effects into account. Markevitch et al. (1994, 1996a) presented results for A2163. The analysis method presented in the latter paper was used for several other published cluster temperature maps (see references in Table 1 below) and is used in this paper. Applying independent techniques, Ikebe et al. (1996, 1997) analyzed the Fornax and Hydra A clusters. Loewenstein (1997) reported preliminary results on A2218; Honda et al. (1996) presented a temperature map of Coma, while Ezawa et al. (1997) reported on the temperature and abundance profile of AWM7. A temperature map of A1367 has been obtained by Donnelly et al. (1997), and a more detailed map of the central part of Coma by Jones et al. (1997).

In this paper, we report on the first systematic study of a representative sample of 26 nearby hot clusters, which we undertaken to determine the common properties of their spatial temperature distributions. Because of the statistical purpose of this investigation, we give only a brief description of individual clusters, some of which will be discussed in more detail in subsequent papers. We concentrate on the cluster-scale temperature structure and only perform the necessary minimum of modeling of such details as cooling flows, point sources in the field, etc. For these components, we allow maximum parameter freedom to obtain model-independent measurements for the main cluster gas. We use  $H_0 = 100h$  km s<sup>-1</sup> Mpc<sup>-1</sup> and  $q_0 = 0.5$ .

## 2. THE SAMPLE

We selected clusters in the redshift interval  $0.04 < z < 0.09$  with 0.1–2.4 keV fluxes greater than  $2 \times 10^{-11}$  erg s<sup>-1</sup> cm<sup>-2</sup> from the *ROSAT* All Sky Survey X-ray-bright Abell cluster sample (Ebeling et al. 1996), and included Triangulum Australis and Cygnus A, missing from the Abell catalog (Abell, Corwin, & Olowin 1989) due to Galactic obscuration. The redshift range

is chosen so that the most distant clusters of the sample are still well resolved by *ASCA*, while for the most nearby clusters, radii of interest ( $0.5 - 1h^{-1}$  Mpc) and the bright cluster cores are covered by the single *ASCA* field of view, so that stray light contamination from outside the field of view of the observation (Ishisaki 1996) does not complicate the analysis. The redshift and flux selection results in 35 clusters; we analyze 26 of them that currently have accessible *ASCA* data (see Table 1). For our present purposes, it is unimportant that the sample is not a complete flux-limited one. Rather, we aim at a representative sample of clusters with a range of temperature and having different evolutionary stages. Our list includes such diverse clusters as A754 which is undergoing a major merger (e.g., Henry & Briel 1995; Henriksen & Markevitch 1996) as well as A1795 and A2029 which are among the most regular X-ray and strongest cooling flow clusters (e.g., Edge, Stewart, & Fabian 1992; Buote & Tsai 1996; Sarazin, Wise, & Markevitch 1997). The sample includes clusters with average temperatures from 4 to 10 keV, with mergers and strong cooling flows at both ends of the temperature interval. In addition to the variety of X-ray morphologies, A780 (Hydra A) and Cygnus A are examples of clusters with powerful central radio sources, while A3558 is located in the dense environment of the Shapley Supercluster (e.g., Etori, Fabian, & White 1997).

## 3. METHOD

The *ASCA* mirrors have an energy-dependent point spread function (PSF) with an average half-power diameter of 3' (Serlemitsos et al. 1995). The PSF effects should be taken into account when deriving spatially resolved temperature distributions (e.g., Takahashi et al. 1995). The method for doing this, which we use here, is described in Markevitch et al. (1996a) and Markevitch (1996, hereafter M96). Here we present its brief outline and relevant additional details. In this paper, we study spatial distributions of projected cluster gas temperatures. For this, we divide each cluster image into regions, usually selected to coincide with interesting surface brightness features, and assume that the spectrum is uniform over each region. Because *ASCA* has insufficient angular resolution to obtain, simultaneously, both surface brightness and temperature distributions with sufficient accuracy for clusters in our sample, we use higher-resolution images from the *ROSAT* PSPC for all clusters except A1650 and A2065, for which *Einstein* IPC and IPC combined with *ROSAT* HRI were used, respectively. These images are used as models of the surface brightness distributions which determine relative normalizations between the projected emission measures in different cluster regions.

*ASCA* spectral data are collected from the regions in the detector plane that correspond to the sky regions, applying the SIS and GIS field of view boundaries. Direct and scattered flux contributions from each sky region to each detector region are calculated by multiplying the model image by the *ASCA* effective area and convolving it with the *ASCA* PSF (both dependent on position and energy) for each energy bin, then integrating the result over the respective detector regions. Then cluster temperatures in all model regions are fitted simultaneously to the spectra from all regions, all detectors, and all pointings if there is more than one.

### 3.1. Brightness Model from *ROSAT* PSPC

We used the Snowden et al. (1994) code to generate *ROSAT* PSPC images in the 0.5–2 keV energy band (or in the 0.9–2 keV

TABLE 1  
CLUSTER SAMPLE

| Name           | Exposure, ks <sup>c</sup> |          | $z$   | $T_e$ single-comp. <sup>a</sup><br>keV | $T_X$ weighted <sup>b</sup><br>keV  | $r_{180}$<br>arcmin <sup>c</sup> | Ref. | Notes <sup>d</sup> |
|----------------|---------------------------|----------|-------|--|-------------------------------------|----------------------------------|------|--------------------|
|                | GIS                       | SIS      |       |  |                                     |                                  |      |                    |
| A85            | 27+14                     | 21+10    | 0.052 | 6.1 ± 0.2                              | 6.9 ± 0.4                           | 38.9                             |      | m, CF              |
| A119           | 32                        | 18       | 0.044 | 5.8 ± 0.6                              | 5.6 ± 0.3                           | 40.5                             |      | m                  |
| A399           | 29+38                     | 22+31    | 0.072 | 7.4 ± 0.7                              | 7.0 ± 0.4                           | 29.2                             |      |                    |
| A401           | 32+38                     | 27+31    | 0.074 | 8.3 ± 0.5                              | 8.0 ± 0.4                           | 30.6                             |      |                    |
| A478           | 33                        | 15       | 0.088 | 7.1 ± 0.4                              | 8.4 <sup>+0.8</sup> <sub>-1.4</sub> | 26.9                             |      | CF                 |
| A754           | 21                        | 16       | 0.054 | 9.0 ± 0.5                              | 9.5 <sup>+0.7</sup> <sub>-0.4</sub> | 44.0                             | 1    | M                  |
| A780 (Hydra A) | 26                        | 23       | 0.057 | 3.8 ± 0.2                              | 4.3 ± 0.4                           | 28.5                             |      | CF                 |
| A1650          | 49                        | 42       | 0.085 | 5.6 ± 0.6                              | 6.7 ± 0.8                           | 24.9                             |      | CF                 |
| A1651          | 32                        | 25       | 0.085 | 6.3 ± 0.5                              | 6.1 ± 0.4                           | 23.7                             |      |                    |
| A1795          | 36                        | 28       | 0.062 | 6.0 ± 0.3                              | 7.8 ± 1.0                           | 35.2                             |      | CF                 |
| A2029          | 34                        | 30       | 0.077 | 8.7 ± 0.3                              | 8.9 ± 1.0                           | 31.2                             | 2    | CF                 |
| A2065          | 23+23                     | 20+21    | 0.072 | 5.4 ± 0.3                              | 5.5 ± 0.4                           | 25.8                             | 7    | M, CF              |
| A2142          | 14+17                     | 9+14     | 0.089 | 8.8 ± 0.6                              | 9.7 <sup>+1.5</sup> <sub>-1.1</sub> | 28.5                             |      | CF                 |
| A2256          | 28+35                     | 21+24    | 0.058 | 7.5 ± 0.4                              | 6.6 ± 0.4 <sup>f</sup>              | 34.4                             | 3    |                    |
| A2319          | 13+15                     | 10+12    | 0.056 | 9.2 ± 0.7                              | 8.8 ± 0.5                           | 41.4                             | 4    |                    |
| A2597          | 39                        | 30       | 0.085 | 3.6 ± 0.2                              | 4.4 <sup>+0.4</sup> <sub>-0.7</sub> | 20.0                             |      | CF                 |
| A3112          | 34                        | 15       | 0.070 | 4.7 ± 0.4                              | 5.3 <sup>+0.7</sup> <sub>-1.0</sub> | 26.0                             |      | CF                 |
| A3266          | 33                        | 24       | 0.055 | 7.7 ± 0.8                              | 8.0 ± 0.5                           | 40.2                             |      |                    |
| A3376          | 21                        | ...      | 0.046 | 4.3 ± 0.6                              | 4.0 ± 0.4                           | 32.9                             |      |                    |
| A3395          | 31                        | 22       | 0.050 | 4.8 ± 0.4                              | 5.0 ± 0.3                           | 34.5                             |      | m                  |
| A3558          | 17                        | 12       | 0.048 | 5.5 ± 0.3                              | 5.5 ± 0.4                           | 37.6                             | 5    | M, CF, $\gamma$ ?  |
| A3571          | 23+19+22                  | 15+15+19 | 0.040 | 6.9 ± 0.3                              | 6.9 ± 0.2                           | 49.9                             |      | CF                 |
| A3667          | 16                        | 13       | 0.053 | 7.0 ± 0.6                              | 7.0 ± 0.6                           | 38.5                             | 7    | M, CF              |
| A4059          | 36                        | 26       | 0.048 | 4.1 ± 0.3                              | 4.4 ± 0.3                           | 33.5                             |      | CF                 |
| Cygnus A       | 29+33                     | 24+25    | 0.057 | 6.5 ± 0.6                              | 6.1 ± 0.4                           | 33.7                             | 7    | M, $\gamma$        |
| Triangulum     | 11+7                      | 9+4      | 0.051 | 9.5 ± 0.7                              | 9.6 ± 0.6                           | 46.7                             | 6    | m; $\gamma$ or CF? |

<sup>a</sup> Single-temperature fit to the spectrum of the whole cluster

<sup>b</sup> Emission-weighted gas temperature excluding cooling flow and other contaminating components, see §5

<sup>c</sup> Estimated from  $T_X$ , see §6

<sup>d</sup> Detected in our temperature data: CF — significant central cool component;  $\gamma$  — central power-law component; M — major merger; m — some indication of merging

<sup>e</sup> Entries with “+” are exposures for multiple pointings

<sup>f</sup> Including secondary cluster. Excluding secondary,  $7.3 \pm 0.5$  keV.

References: 1—map presented in Henriksen & Markevitch (1996); 2—Sarazin et al. (1997); 3—M96, MV97b; 4—map in M96; 5—MV97a; 6—map in MSI; 7—maps in M98.

band for clusters with the highest Galactic absorption to maximize the signal to noise ratio). An X-ray background was determined for each cluster individually by fitting the outer radii of the PSPC field of view by a constant plus a power law cluster radial brightness profile. All clusters in our sample are sufficiently small so that separating the outer cluster halo and the background did not pose a problem. The *ROSAT* band X-ray background averaged over areas similar in size to the regions of our temperature maps ( $\sim 10'$  in diameter) has an rms scatter of about 10%, while the background averaged over larger areas similar to the outer bins of our radial temperature profiles ( $\sim 30-40'$ ) has a scatter of 5% (Vikhlinin & Forman 1995; Soltan et al. 1996). These estimates of the PSPC background uncertainty are included in our confidence intervals.

There is an ambiguity in defining a background when a significant fraction of it is resolved into point sources. Hard point sources that are bright in the *ASCA* band were fitted individu-

ally along with the surrounding cluster temperatures, to account for their scattered flux. Softer sources that are bright only in the *ROSAT* band were excluded from the fit by masking them from the model and detector regions. Otherwise, they may lead to an overestimate of the emission measure in the outer, low surface brightness regions of the cluster, resulting in a slightly lower best-fit *ASCA* temperature. Given the limited *ASCA* resolution, it is not practical to excise all point sources detectable in the *ROSAT* image, therefore the integral contribution of the remaining numerous weak sources should be subtracted as part of the background. We have calculated the *ROSAT* background consistently with this requirement, by excluding from the background calculation region only sources as bright as those excluded from the *ASCA* fitting region.

### 3.2. *ASCA* PSF Model and Choice of Energy Band

Above 2 keV, the *ASCA* PSF is modeled by interpolating between the Cyg X-1 GIS images at different focal plane positions (Takahashi et al. 1995; Ueno 1996). At lower energies, Cyg X-1 appears intrinsically extended and is inadequate for PSF modeling. In this work, we use *ASCA* data in the 1.5–11 keV band, excluding the 2–2.5 keV interval with a poorly calibrated effective area, and extrapolate the PSF model from higher energies to the 1.5–2 keV interval (assuming a higher PSF uncertainty of 10%). We have chosen to include the latter interval despite the increasing PSF uncertainty in order to take advantage of the high statistical precision data below the 2.2 keV mirror reflectivity edge. Another reason for including it is that for many clusters, we found that discarding lower energy data resulted in slightly higher (by about 0.5 keV) temperatures. This can be expected given that the effective area calibration is more accurate over the whole *ASCA* energy band than in any smaller interval. Even though this difference is smaller than most individual temperature uncertainties, we tried to avoid such a bias. For a check, we analyzed all observations with the energy cut-off at 1.5 and 2.5 keV and found no significant differences in best-fit temperature values except for that mentioned above.

For modeling of the SIS data, the GIS Cyg X-1 calibration images were corrected for the energy dependence of the intrinsic GIS detector blurring by additional smoothing resulting in a final constant resolution (Gaussian  $\sigma = 0.5'$ ). The cluster SIS data also were smoothed to the same resolution.

### 3.3. Treatment of Cooling Flows

In this work, cluster cooling flows are considered “contaminants” whose effect on the measured temperatures of the main cluster gas should be removed. Usually we can confidently detect the presence of an additional spectral component at the center of a cooling flow cluster, but in most cases we cannot say whether it is a cooling flow, an additional lower single-temperature, or a power law component without a detailed analysis (e.g., of spectral lines and the surface brightness) which is beyond the scope of this work. The best-fit temperatures in the outer cluster regions are essentially independent of these details, as long as our chosen model describes the central spectrum adequately and the relative normalization of the central and the outer regions is correct.

Due to the spectral complexity of cooling flows, the relative emission measure of the central cluster region calculated from the *ROSAT* PSPC image (as is done for other regions) is inadequate. For this reason and to allow maximum model independence, we fitted, as free parameters, the normalization of the central region relative to other regions, the fraction of a cooling flow (or another spectral component) in the total emission from that model region, and the temperature of its main thermal component, from which the cooling was assumed to start. A cooling flow spectrum was modeled as prescribed in Sarazin & Graney (1991). Because of the large number of free parameters for the central spectra and the PSF uncertainty associated with the small regions ( $r = 1.5'$  or  $2'$ ) used to model cooling flows, the derived central temperatures for strong cooling flow clusters are weakly constrained. Generally, the cooling flow model parameters are not usefully constrained and therefore are not presented.

Bright point sources that are seen both in *ROSAT* and *ASCA* images were fitted following the same procedure.

### 3.4. Data and Model Coordinate Alignment

It is important that the model image, derived from *ROSAT* or *Einstein*, is accurately aligned with the *ASCA* image. A small offset can result in an error of the model flux in the regions surrounding the brightness peak that is greater than the statistical uncertainty, especially for clusters with strong cooling flows. The standard *ASCA*  $1\sigma$  coordinate accuracy of  $24''$  (Gottlieb 1996) is insufficient for this purpose. Therefore, we corrected the *ASCA-ROSAT* coordinate offset for each individual observation by comparing the *ROSAT* image (convolved with the *ASCA* PSF) to the actual *ASCA* image. The uncertainty of such corrections is  $6\text{--}13''$  ( $1\sigma$ ), depending on how peaked the cluster is.

In the course of this work we also have noticed a systematic  $0.4'$  offset between the GIS and SIS detector coordinates. For the same reason as above, this offset can result in an inconsistency between the GIS and SIS temperature maps of cooling flow clusters. We corrected this offset; our previous papers did not consider strong cooling flows and therefore were not significantly affected.

### 3.5. ASCA Data Filtering and Background Calculation

We have applied a conservative version of the standard filtering criteria to the *ASCA* data (ABC Guide). In addition, SIS data that showed telemetry saturation were excluded. The resulting exposures (averages of two SISs and two GISs) are presented in Table 1. For the GIS, we used only the data within  $18'$  of the detector centers, and corrected the detector gain maps for their long-term time dependence (Makishima 1996). For the SIS, we analyzed faint and bright mode data and different clocking modes together. Our results are insensitive to the time dependence of the SIS spectral resolution, and a 1.5 keV energy cutoff ensures that they are also insensitive to the uncertainty of the SIS efficiency at the energies below  $\sim 0.8$  keV (e.g., Sarazin et al. 1997).

For the background calculation, we used *ASCA* observations of blank fields. For the SIS, the normalization was calculated using the total useful exposure, applying a correction for the long-term mode-dependent degradation of the SIS efficiency (Dotani et al. 1995) since the background fields were observed early in the mission. A  $1\sigma$  uncertainty of 20% was assumed for the SIS background normalization.

For the GIS, the blank field data were normalized by exposures in the individual cut-off rigidity intervals as a first approximation. For the smaller and fainter clusters in our sample, it was possible to model and subtract the cluster emission from the same GIS image in the hard energy band (where the cluster is faint and at the same time the background is most important), and normalize the blank field background to the residual. An uncertainty of such normalization was 5–7% ( $1\sigma$ ). The normalization determined in such a way showed good agreement with that determined from the exposure values, with a typical deviation of less than 10%. We therefore assumed a 10%  $1\sigma$  uncertainty for bright clusters for which such a direct background estimate was impossible.

### 3.6. Summary of Systematic Uncertainties

To summarize, the following systematic uncertainties ( $1\sigma$ ) were included in our temperature confidence intervals in addition to the statistical uncertainties:

GIS and SIS background normalization errors of 5–20%;

An *ASCA* effective area calibration uncertainty of 5% of the model flux in each energy interval (this incorporates the uncertainty of the mirror optical axis positions, see Gendreau & Yaqoob 1997);

A PSF error of 10% for radial temperature profiles, of 10% for temperature maps in the PSF core for relatively small regions (e.g., cooling flows), and of 15% for temperature maps in the wings of the PSF;

A *ROSAT* surface brightness model error, including the *ROSAT* statistical error and background uncertainties of 5% for the temperature profiles and 10% for the temperature maps;

A 6–20'' relative *ASCA-ROSAT* image offset uncertainty.

Effects of the PSF, effective area and *ASCA* background uncertainties on the spatially-resolved temperature values obviously are reduced when the cluster is observed in several offset pointings, ideally with different telescope roll angles, because possible spatially dependent miscalibrations then average out. Ten clusters in the sample have multiple pointings, of them A2256, A3571 and Cygnus A have been observed with different roll angles. Use of all four *ASCA* detectors also reduces the effects of PSF and effective area errors, since the mirror optical axes are offset by a few arcminutes with respect to each other.

The PSF scattering seriously complicates our measurements. In the outermost radial bins of our clusters, only 30–60% of the flux at an energy of 5 keV originates in the corresponding region in the sky, while the remaining flux is that scattered from the bright inner cluster regions. We will see below that for the distant cooling flow clusters that have sharp central brightness peaks and therefore the greatest scattered fraction, the PSF uncertainty translates into large uncertainties in the outer temperatures. This usually precludes the reconstruction of accurate two-dimensional temperature maps.

### 3.7. Fitting Procedure

The GIS and SIS spectra from each detector (SIS chips were treated as independent detectors) were binned in several (5–13) intervals with different width so that  $\chi^2$  minimization could be performed. To avoid finding false minima of  $\chi^2$  as a function of many free parameters, we used the annealing minimization technique (e.g., Press et al. 1992). The Raymond & Smith (1977, 1992 version) model for thermal emission was used. In most cases, abundances in different regions were not usefully constrained and therefore were fixed at the cluster average values. Given the *ASCA* spectral resolution, this practically does not affect the obtained best-fit temperature values.

Generally, we used spectra from all detectors for each region to reduce systematic uncertainties. We excluded from the fit the spectra with insufficient statistics, for example, due to the partial coverage when a given region is better covered by another pointing, or due to the SIS small field of view when the GIS has sufficient data for this region. When fitting the temperature maps, we also excluded SIS spectra for regions with small partial chip coverage to avoid problems due to the possible temperature nonuniformity inside each region. Normalizations between different detectors were free parameters, while relative normalizations between different model regions were fixed or freed as described above. Due to our rather conservative inclusion of systematic uncertainties, values of  $\chi^2_{\min}$  per degree of freedom were less than 1 in all fits. One-parameter confidence intervals for the fitted parameters were estimated by Monte-Carlo simulations that included all statistical and systematic uncertainties.

For a consistency check, we fitted GIS and SIS data and different pointings separately, finding reasonable agreement in all cases but one. For A3376, we were unable to obtain consistent results from GIS and SIS, most likely due to the anomalous SIS background in that observation, and chose to use only the GIS data. Results of separate fits for different pointings at the same cluster were consistent within their expected errors, confirming the adequacy of the adopted systematic error estimates.

## 4. RESULTS

### 4.1. Wide-beam Temperatures

To check the consistency between our results and earlier wide-beam measurements, we have performed single-temperature fitting of the overall cluster spectra (for  $r < 16$ – $18'$ ) without exclusion of point sources (except for Cygnus A which was fit by a thermal plus an absorbed power law component) or use of cooling flow models. GIS and SIS data were fitted simultaneously, except that SIS data were not used when it was observing in 1-CCD mode with a field of view of only  $11' \times 11'$  (A1650, A3266, Triangulum Australis). Absorption columns were fixed at their Galactic values taken from Dickey & Lockman (1990). The resulting temperature values are given in Table 1. Fig. 1 shows these values compared to those from David et al. (1993), who presented wide-beam *Einstein* MPC results and compiled the most accurate *EXOSAT* (Edge & Stewart 1991) and *Ginga* (Hatsukade 1989) measurements. We added a later Cygnus A *Ginga* result from Ueno et al. (1994). Only those David et al. values with an accuracy of better than 50% are shown. For several clusters where MPC and either *EXOSAT* or *Ginga* marginally disagreed, both measurements are shown.

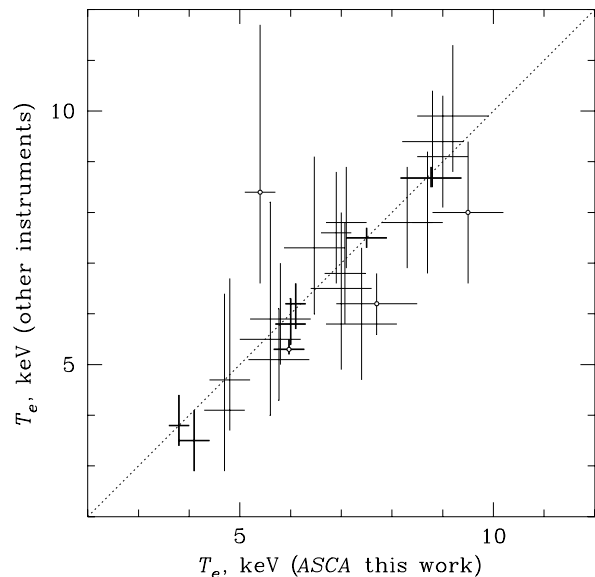


FIG. 1.—Comparison of our temperatures with those from *Einstein* MPC, *EXOSAT* and *Ginga* (David et al. 1993; Ueno et al. 1994). Errors are 90%. Values from more than one earlier instrument are shown if they disagreed. Bold crosses denote the most accurate of the David et al. values. Circles denote the most notable discrepancies, discussed in text.

The figure shows that over the whole range of temperatures in the sample, our temperatures are in good agreement with pre-

vious measurements. The most notable exceptions, marked by circles, merit explanation. The highest-temperature deviation is Triangulum Australis, whose *EXOSAT* temperature is lower than ours. Markevitch, Sarazin, & Irwin (1996b, hereafter MSI) showed that most of this discrepancy is caused by different assumed  $N_H$  values (Edge & Stewart obtained a best-fit  $N_H$  value higher than Galactic; however, *ROSAT* PSPC observations yielded a value very close to the Galactic value which we use). Also, an update of the GIS gain calibration (Makishima 1996) has resulted in a slightly lower *ASCA* temperature than the one reported in MSI. Further, our 7.7 keV temperature for A3266 is inconsistent with the lower MPC value. A soft point source seen in the *ROSAT* PSPC image just outside our fitting region (see Fig. 2) may contribute to this discrepancy. Our 6.0 keV value for A1795 is higher than the *Ginga* value but agrees with the MPC value (the MPC and *Ginga* values are themselves discrepant). This cluster has a strong cooling flow and instruments with different energy coverage are likely to obtain different single-temperature fits. As expected, our single-temperature fit for A1795 depends on the adopted low energy cutoff. The energy band difference between *ASCA* and the MPC may also be the reason of the A2065 discrepancy. For this cluster, we obtain  $T = 5.4$  keV but also detect large spatial temperature variations probably due to a merger (Markevitch et al. 1998, hereafter M98). The separate GIS and SIS single-temperature fits are similar, and it is noteworthy that our A2065 temperature is in a better agreement with the  $L_x - T$  relation (David et al. 1993) than the higher MPC value.

Having performed this consistency check, we show below that single-temperature values often have little meaning, because clusters are nonisothermal and many have strong cooling flow contributions.

#### 4.2. Temperature Maps and Radial Profiles

Figures 2 and 3 present two-dimensional temperature maps for 9 clusters with superposed *ROSAT* PSPC brightness contour maps. We show only clusters for which the temperature maps have useful accuracy. Temperature maps obtained for A754, A2029, A2065, A2256, A2319, A3558, A3667, Cygnus A, and Triangulum Australis are published separately (see references in Table 1). In Figs. 2 and 3, we tried to assign different shades of gray to significantly different temperatures, but it was not always possible due to the very different confidence intervals. Individual clusters are discussed in the section below.

Figure 4 shows radial projected temperature profiles for all clusters in our sample except for the previously published A2029, A2256, A2319, and A3558 (see references in Table 1) and A2597 which is dominated by a cooling flow (see below). The profiles were obtained in the annuli around the centroid of the large-scale emission, which did not always coincide with the brightness peak (an extreme example is the double cluster A3395, see Fig. 3). Generally, we did not exclude from the radial profiles any substructures (except for the contaminating point sources) even when they were obvious, in order to be able to compare these results to the future low statistics data on distant clusters.

#### 4.3. Results for Individual Clusters

A85.—A temperature map is reconstructed in the annuli  $r = 0 - 1.5' - 6' - 12' - 20'$ , with the second and third annuli divided into 4 equal sectors and the outermost annulus in two unequal

sectors (Fig. 2). Sectors 6 and 10 coincide with an infalling subcluster (e.g., Durret et al. 1997). In the center, we detect a strong cooling flow with greater than 99.9% confidence; a single-temperature fit is shown in the map and the upper temperature of a cooling flow is shown in the radial profile in Fig. 4. The temperature declines with radius, and the map shows no highly significant deviations from azimuthal symmetry. However, if the less massive infalling subcluster were only a projection, the correspondent sectors would appear cooler than adjacent regions (as, for example, in A2256 or A2319, M96). Instead, the map and the profile (Fig. 4) show that the subcluster regions are probably hotter than the adjacent ones, suggesting the presence of shock-heated gas arising from an ongoing collision. A more detailed temperature map, e.g., from *AXAF*, should detect such shocks.

A119.—The temperature map is reconstructed on a grid of  $6' \times 6'$  boxes, with regions 1 and 2 composed of 2 boxes and region 15 of 4 boxes for better accuracy. Region 10, coincident with one of the infalling or projected subclusters seen both in the X-ray image and in the optical data (Way, Quintana, & Infante 1997), is significantly cooler than the cluster average. Region 13, located apparently “in front” of this subcluster, is marginally hotter than the cluster average, suggesting that there indeed is a mild merger shock and therefore simple projection is unlikely. Our map excludes the possibility of a major merger comparable to the ones seen in A754, A3667 or Cygnus A. The radial temperature profile of this cluster is nearly constant with a probable mild central peak.

A399–A401.—*ASCA* observed this pair with 3 pointings centered at each cluster and between them. Our regions for A401 are sectors of concentric annuli with  $r = 0 - 2' - 7' - 14'$ . In the A399 map, the regions are the same except that the innermost one is centered on the brightness peak while others are centered on the cluster centroid. The overall temperatures for A401, A399, and the link region are in agreement with the earlier *ASCA* analysis of Fujita et al. (1996) that did not take into account the PSF effects. Our analysis ignores the effects of *ASCA* stray light (Ishisaki 1996) that may be important when a bright cluster is just outside the mirror field of view, as in two of these three pointings. However, an estimate shows that such contamination is comparatively small for these observations.

The temperature map shows a centrally symmetric temperature structure in both clusters, with sectors 6 and 16, each pointing toward the opposite cluster, being hotter, with marginal significance, than the corresponding sectors at the same radius. The temperature declines with radius, with peaks in the centers of both of these cD clusters. Despite the large uncertainty, the gas in region 10 between the clusters does not seem to follow the temperature decline, arguing against projection and possibly suggesting the beginning of a collision of these clusters or a massive dark matter filament between them. Our analysis requires no cooling flow components in these clusters, in agreement with Edge et al. (1992). This makes A401 a rather unusual cD cluster since neither the temperature map nor the X-ray image indicate recent merger activity in the central regions of this cluster, and yet it has no cooling flow.

A478.—This distant cluster has a strong cooling flow (e.g., White et al. 1994) and is at the limit of the *ASCA*'s angular resolution. For this reason, reconstruction of its two-dimensional map is currently impossible and even a radial profile (for which we use radii  $r = 0 - 1.5' - 6' - 16'$ ) has very large uncertainties (Fig. 4). We fixed the central temperature, which is also a cool-

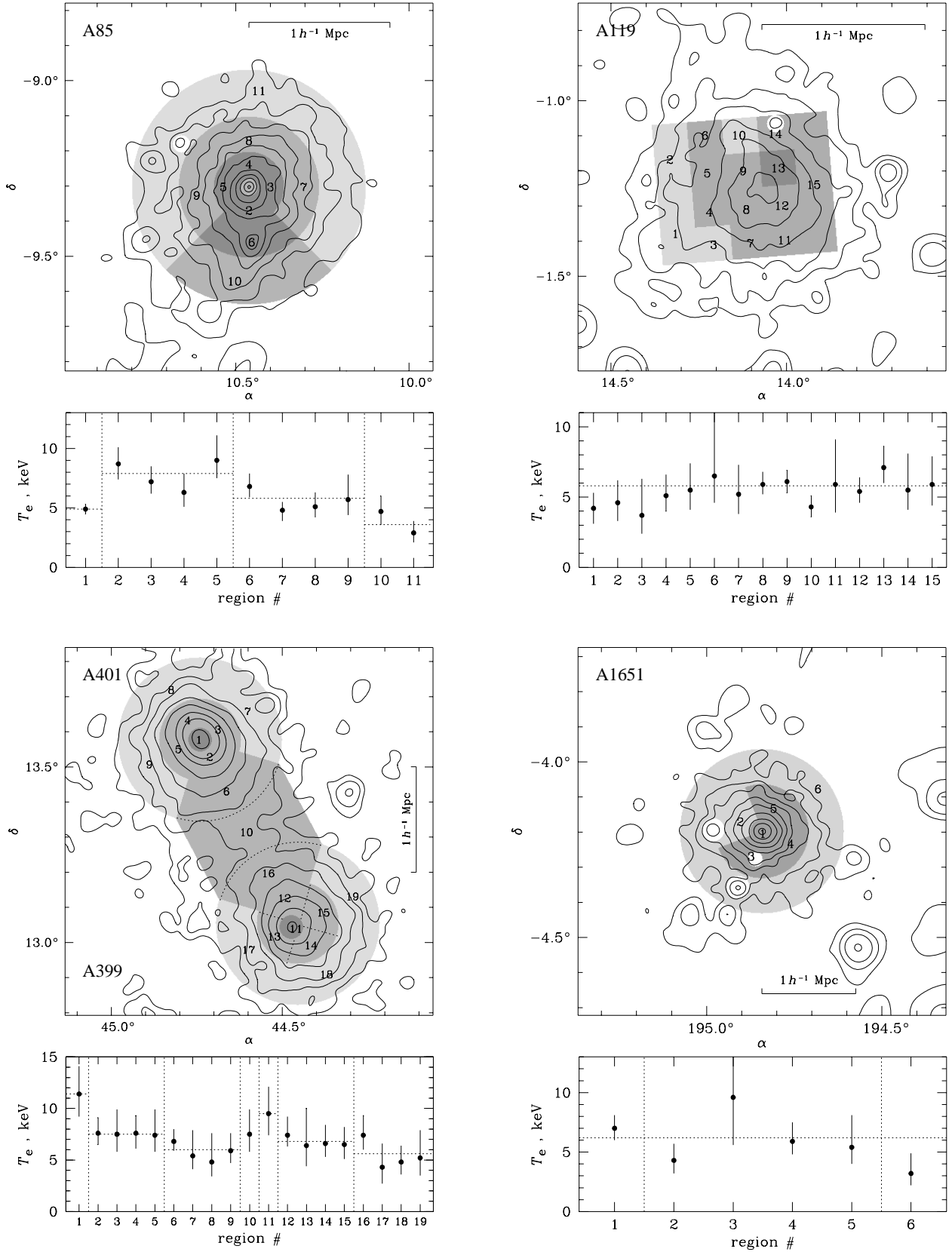


FIG. 2.—Cluster temperature maps. Contours show *ROSAT* PSPC brightness, grayscale shows *ASCA* temperatures. Regions (sectors, boxes, or their combination, delineated by dotted lines in the nonobvious places) are numbered and their temperatures with 90% confidence intervals (including systematics) are shown in the lower panels. Dotted horizontal lines in lower panels show emission-weighted average temperatures either in the annulus or over the whole cluster. Point sources excluded from the fits are shown as blank circles, but some of them are not shown for clarity.

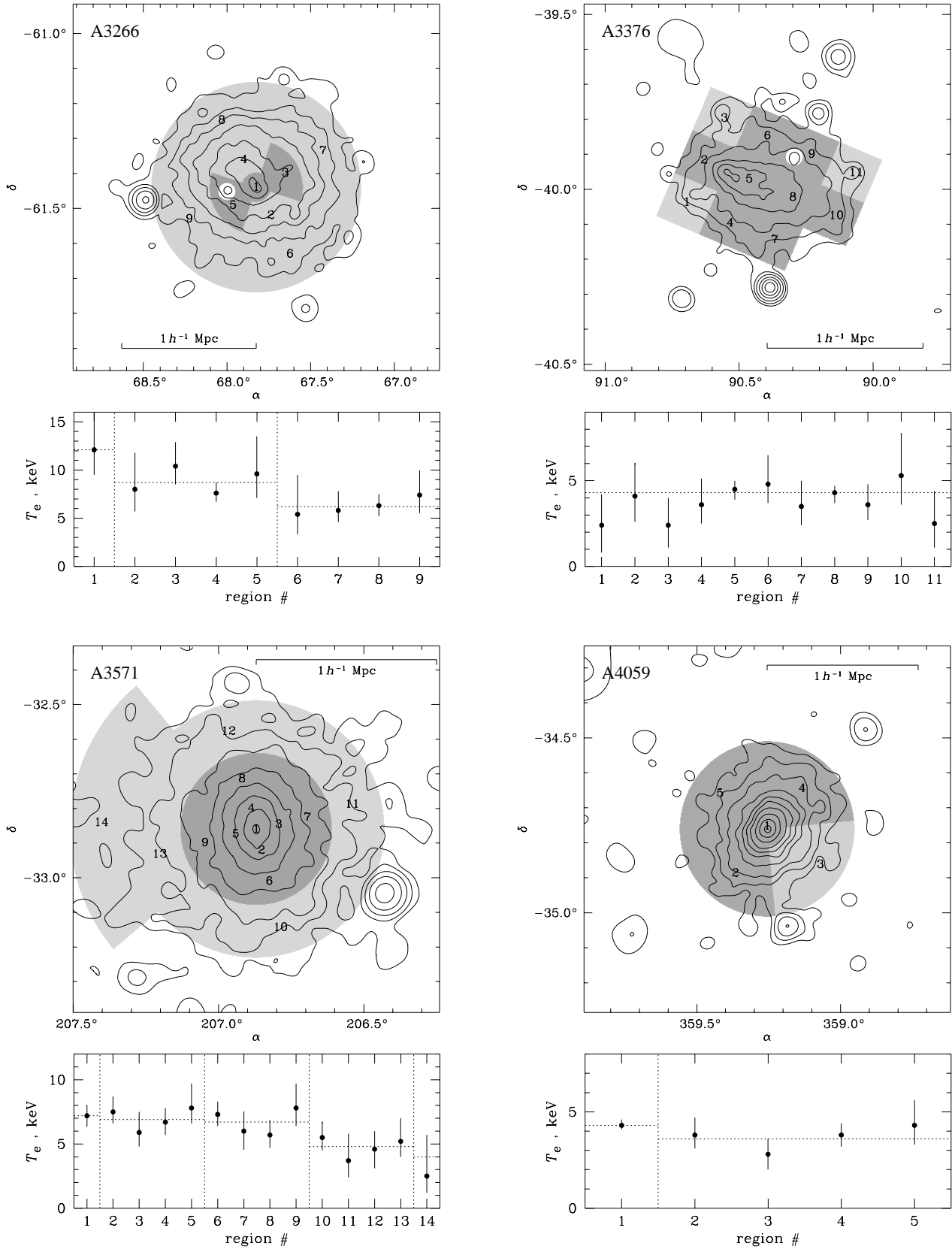


FIG. 2.—Continued

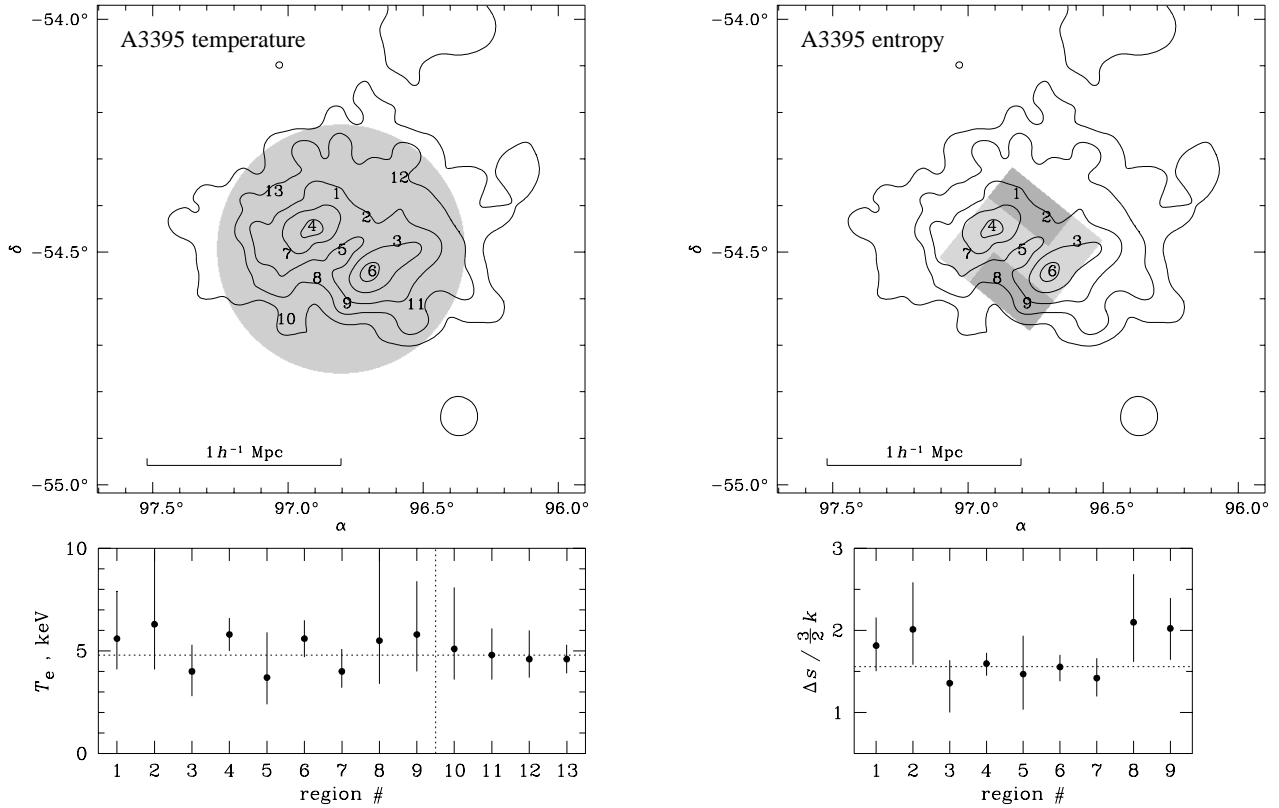


FIG. 3.—Temperature and specific entropy maps of A3395 (see text). Left panels are similar to Fig. 2. Lower right panel shows approximate specific entropy in each region with respect to an arbitrary zero value; horizontal line denotes a weighted mean value. Grayscale in the upper right panel shows these specific entropy values overlaid on the image.

ing flow upper temperature, to be equal to that in the surrounding annulus. A central cool component is required at 94% confidence and there is a marginally significant temperature decline with radius.

*A754*.—A temperature map of this merging cluster was discussed in detail in Henriksen & Markevitch (1996). Here we present its radial temperature profile, although for such a highly asymmetric cluster with complex temperature structure, it does not have much meaning. The profile shows a temperature decline.

*A780 (Hydra A)*.—Ikebe et al. (1997) previously analyzed the same data on this cooling flow cluster with their independent code. We find a temperature decline with radius outside the central cluster region similar to that in Ikebe et al., and also detect the presence of cooler gas in the center at greater than 99.9% confidence. A two-dimensional temperature map of this cluster is not given since it would be inaccurate because of the strong cooling flow.

*A1650*.—This is another example of a distant cooling flow. Our analysis of this cluster with a large cD was complicated by the absence of a PSPC image. Instead, we used the lower-resolution *Einstein* IPC image. As a result, the accuracy of the temperature profile is poor. A cool central component is detected at 99% confidence.

*A1651*.—This is a distant cD cluster, for which our data do not require a central cool component. Its PSPC image is rather regular and our temperature map ( $r = 0-2'-8'-14'$  annuli with the second annulus divided into 4 sectors) shows no interesting

structures, although its accuracy is poor. A radial temperature decline is suggested.

*A1795*.—This cluster has one of the strongest known cooling flows (Edge et al. 1992; Fabian et al. 1994a [an earlier *ASCA* analysis]; Briel & Henry 1996). The cool component is required at greater than 99.9% confidence in the central  $r = 1.5'$  region. This small central region contains almost half of the total cluster emission in the *ROSAT* band, which makes our *ASCA* spatially resolved analysis very uncertain. We detect some indication of a radial temperature decline. A bright point source  $6'$  from the center was fit separately and found to be equally well described by either a thermal or a soft power law spectrum; this uncertainty does not affect the temperature values in other cluster regions.

Note that our temperatures at all radii are higher than the single-temperature fit to the overall spectrum (Table 1); this cluster is the most prominent example of how the presence of a strong cooling flow results in an underestimate of the cluster temperature. This issue will be discussed below.

*A2029*.—This strong cooling flow and well relaxed cluster is discussed in detail in Sarazin et al. (1997), who detect a significant radial temperature decline in it.

*A2065*.—A temperature map for this cluster is presented and discussed in M98. A prominent asymmetric temperature pattern is detected, as well as a central cool component (at 99% confidence) which must have survived the ongoing major merger. In Fig. 4, we present its radial temperature profile, which is declining with radius. Dashed cross shows a single-

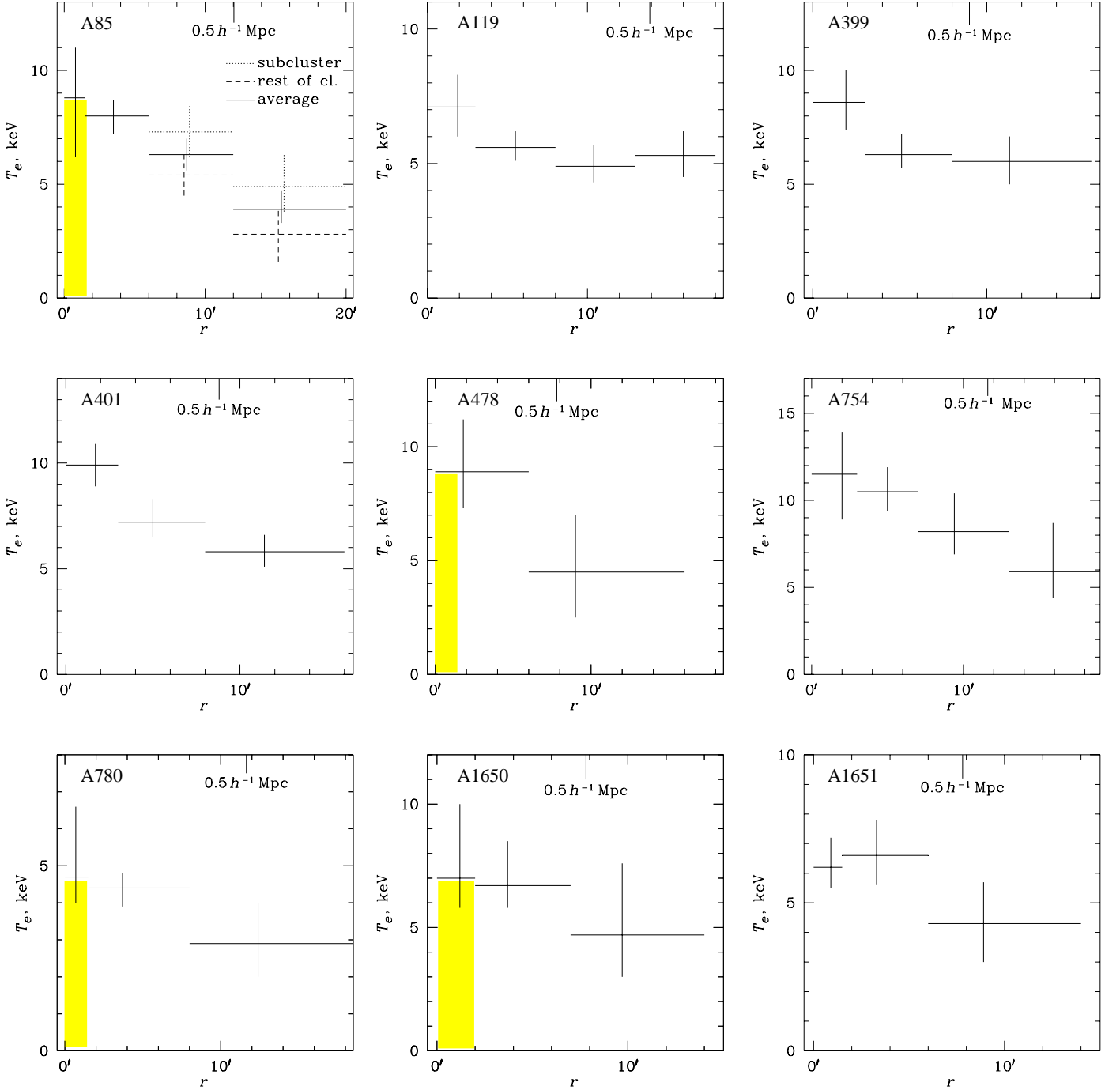


FIG. 4.—Radial projected temperature profiles. Crosses are centered on the emission-weighted radii. Vertical errors are 90% and include systematic uncertainties; horizontal error bars show the boundaries of the annulus. Gray bands denote a continuous range of temperatures in a cooling flow in those clusters where this spectral component is significantly detected by our analysis.

temperature fit in the central bin.

**A2142.**—This is the most distant cluster in our sample. Its *ROSAT* PSPC and HRI images suggest an ongoing merger. However, we cannot reconstruct its temperature map due to the presence of a cooling flow (Edge et al. 1992; Henry & Briel 1996) which we detect with greater than 99% confidence. An AGN  $4'$  from the cluster center is fitted separately by a power law with the best-fit index of  $-1.9$ . The temperature profile has large uncertainties and is consistent with a constant value, al-

though a temperature decline with radius is suggested.

**A2256.**—A detailed discussion of this cluster, including its total mass derivation, is presented in M96 and Markevitch & Vikhlinin (1997b, hereafter MV97b). Those works inferred that, most probably, the two large subclusters of A2256 have not yet started interacting. An ongoing collision between them is excluded, since the temperature map does not exhibit structures characteristic of shock heating, predicted by simulations and indeed observed in several merging clusters such as A754

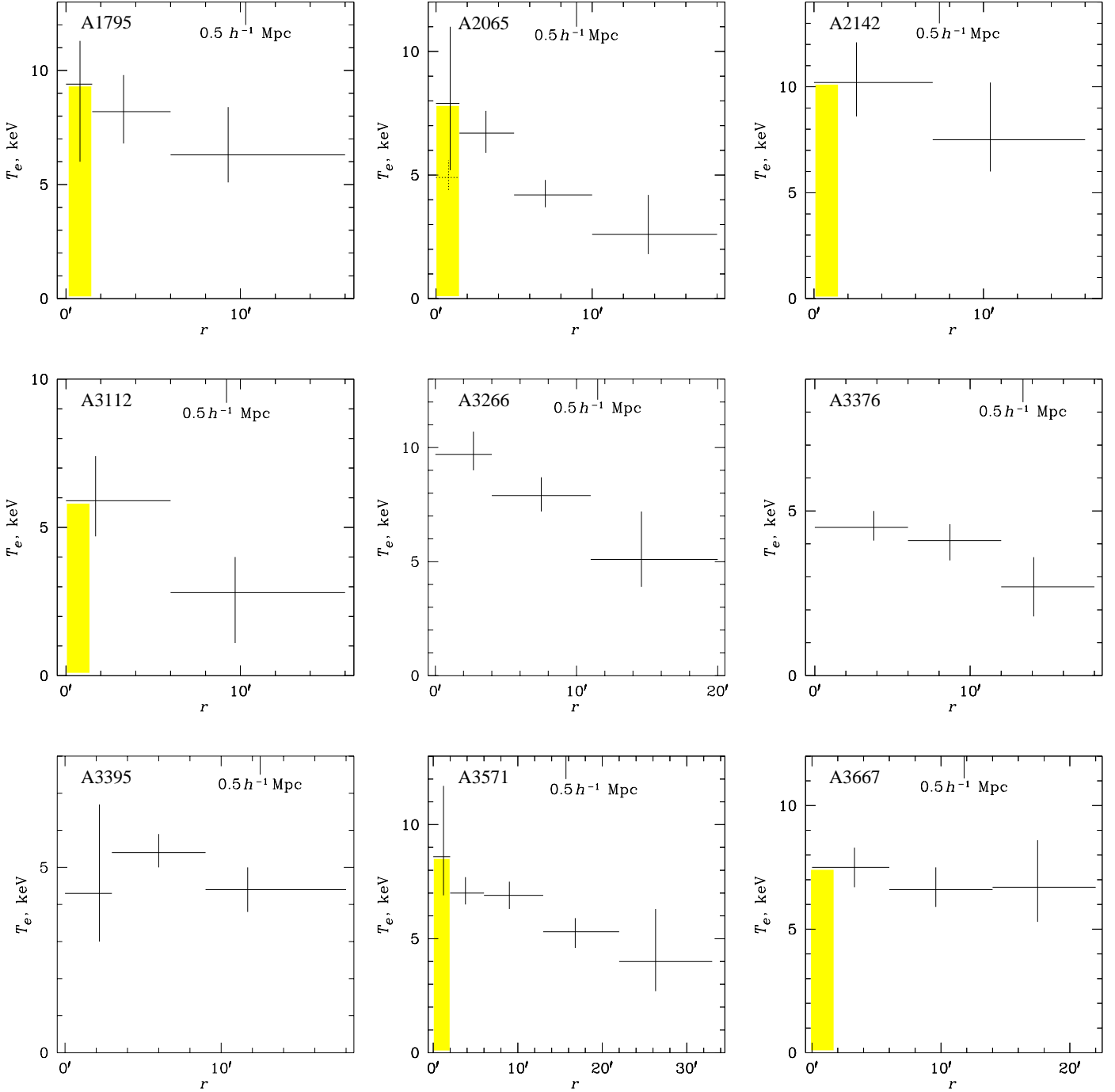


FIG. 4.—Continued

and Cygnus A. In the discussion below, we use the projected temperature profile for the main component of A2256 obtained in MV97b.

A2319.—GIS results for this cluster were presented in M96. The GIS+SIS results are similar with a small revision of the overall temperature (Table 1). M96 found that there is a cool region near the center coincident with a subcluster seen in the X-ray image. As for A2256, the temperature map does not suggest any major merger, although it has a poorer accuracy than the A2256 map.

A2597.—This is a distant cluster dominated by a cooling flow (e.g., Edge et al. 1992; Sarazin & McNamara 1997). Almost half of the total emission in the *ROSAT* band originates from the central  $r = 50 h^{-1}$  Mpc ( $0.8'$ ) region. For this reason, we were only able to fit spectra in two radial bins,  $r = 0 - 1.5' - 15'$ , to separate the cooling flow from the rest of the cluster. The cooling flow sufficiently dominated the central bin that we could not determine an independent temperature there, so we assumed that the ambient temperature was constant at all radii. A cool component is required at greater than 99% confidence in the central region.

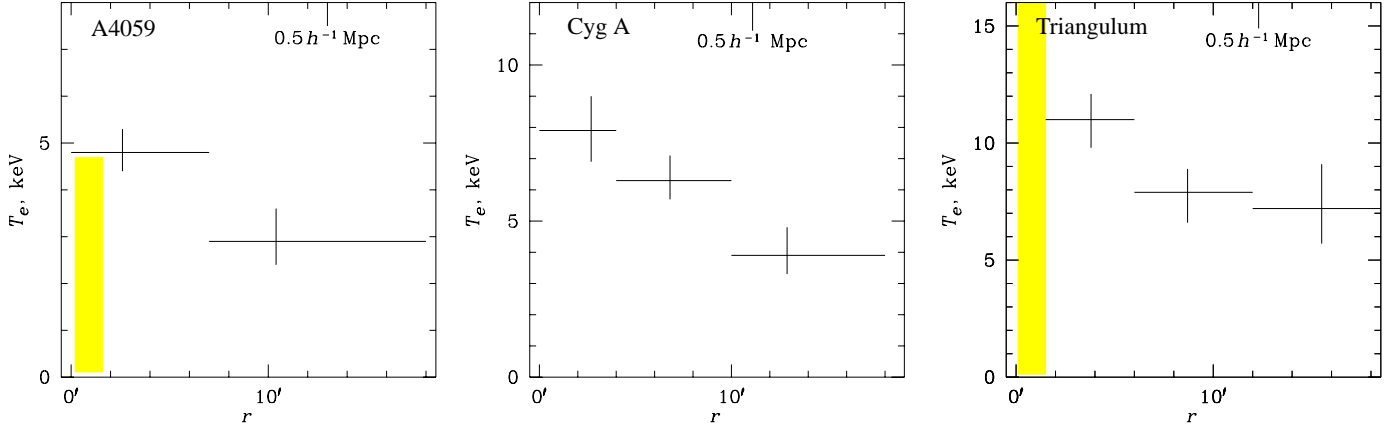


FIG. 4.—Continued

*A3112*.—This cluster possesses a strong cooling flow (Edge et al. 1992) which we detect at 98% significance. Again, for this reason, the radial temperature profile has a large uncertainty. Still, there is a significant indication of a radial temperature decline.

*A3266*.—A *ROSAT* PSPC image of this cluster indicates ongoing merger. Our temperature map (which consists of sectors of annuli with  $r = 0 - 2.5' - 8' - 18'$  centered on the brightness peak, Fig. 2) does not have sufficient resolution, but may indeed suggest an asymmetric temperature pattern expected for a merger. Sector 4, which is coincident with an infalling subcluster, is cooler than the annulus average, while the neighboring sector 3 is hotter, although with only marginal significance. The cluster brightness peak is hot; on average, the temperature declines with radius.

*A3376*.—A temperature map of this cluster (made of  $8' \times 8'$  boxes) is shown in Fig. 2. A comet-like shape of the *ROSAT* image indicates a merger. However, our temperature map probably excludes any strong shocks. A radial profile shows that the outer cluster regions are significantly cooler than the center, although a radial profile has little meaning for this asymmetric cluster. This object is at the lower flux limit of our sample and only has a short GIS exposure, so our results are limited by statistics.

*A3395*.—A temperature map of this double cluster is shown separately from others in Fig. 3. Regions of the map are nine  $5' \times 5'$  boxes, with boxes 4 and 6 coincident with the peaks of the two subclusters, and four sectors of an  $r = 16'$  circle outside the boxes. The temperature map excludes the presence of a very hot gas between the cluster peaks (region 5) which one would expect if the two clusters were colliding head-on. The peaks (regions 4 and 6) are marginally hotter than the cluster average, but temperatures in other regions are consistent with the average within their large uncertainties. The uncertainties are large mostly because of the low statistics of the *ROSAT* PSPC image obtained from a very short (2 ks) exposure.

A closer look at the elongated X-ray images of each of the two *A3395* components suggests that they may in fact be in the course of an offset merger, with the northeast and southwest peaks moving west and east, respectively. Interestingly, the statistically insignificant positive temperature deviations are observed in regions 1, 2, 8, and 9 “in front” of the subclusters if this speculation is correct. Entropy maps are a sensitive indi-

cator of shock heating (MSI) and may reveal additional detail. We show in Fig. 3 (right panel) approximate specific entropies of the gas in the inner 9 cluster regions. The entropy per particle is defined here as  $\Delta s \equiv s - s_0 = \frac{3}{2}k \ln [(T/T_0)(\rho/\rho_0)^{-2/3}]$ , where the subscript 0 refers to any fiducial region in the cluster. For a qualitative estimate, we approximate  $\rho/\rho_0 \sim (S_x/S_{x0})^{1/2}$ , where  $S_x$  is the cluster X-ray surface brightness in a given region. This approximation is adequate in the central regions but is inaccurate in the outer image regions which are not shown (the entropy values there are higher than in the center as in any isothermal cluster). With marginal significance, regions 1, 2, 8, and 9 have higher specific entropy than other central regions which appear to be approximately adiabatic. Note that region 5, between the peaks, has a low density similar to those in high-entropy regions, but has an average entropy. Such an entropy distribution suggests the presence of shock-heated gas in front of each of the two subclusters, which should then indeed collide as proposed above. We note that, of course, dividing temperatures by a power of surface brightness to calculate entropy does not increase the statistical significance of the observed temperature structure, but it helps to present it in a more illuminating way. From the observed entropy differences one can estimate, for example, the relative velocity of the colliding subclusters; however, any quantitative analysis must wait for more accurate measurements.

*A3558*.—This cluster is analyzed in MV97a, who detected temperature structure indicating a major merger, and a slow radial temperature decline. The region around the central galaxy requires a cool and a hot or nonthermal component.

*A3571*.—This cluster has the best-quality data in our sample. Temperatures are obtained in  $90^\circ$  sectors for annuli with  $r = 0 - 2' - 6' - 13' - 22' - 35'$ . In the last annulus, only two sectors are covered by *ASCA*; in one of them, the individual temperature is not usefully constrained and is not shown in Fig. 2, but it is included in the calculation of the radial profile. The map in Fig. 2 shows no significant deviations from azimuthal symmetry, except for the possibility that the southern half of the cluster may be slightly hotter than the northern half. Together with the symmetry of the cluster image, the featureless temperature map suggests that *A3571* is a well-relaxed cluster. This cluster is known to have a small cooling flow (Edge et al. 1992); a central cool component is detected with 92% confidence in our data. The radial temperature profile, shown in Fig.

4, is the most accurate cluster profile published. This profile will be used for a derivation of the total mass profile in a separate paper.

*A3667*.—A temperature map of this cluster shows an ongoing major merger and is presented and discussed in detail in M98. A trace of cooler gas, which must have survived a merger, is detected in the vicinity of the central galaxy with 95% confidence. The radially-averaged temperature profile (Fig. 4) is constant; however, a radial profile has little meaning for this highly asymmetric cluster.

*A4059*.—This is a cooling flow cluster (e.g., Huang & Sarazin 1998); we detect a central cool component with 99% confidence. A crude temperature map (which consists of two annuli with  $r = 0-3'-16'$  with the outer one divided into 4 sectors) shows no significant detail. A single-temperature fit for the central region is shown in the map. A radial profile shows a significant temperature decline with radius.

*Cygnus A*.—A temperature map of this cluster is presented in M98. The map reveals temperature structure indicating an ongoing merger of two large subclusters seen in the X-ray image (and perhaps in the optical as well; Owens et al. 1997), one of which harbors a strong radio galaxy Cygnus A. There is a strong point source at the position of Cygnus A in the hardest-band *ASCA* images where the surrounding cluster emission is faint, which shows that *ASCA* can confidently separate the AGN component from the cluster. Fitting the cluster temperatures simultaneously with a self-absorbed power law in a  $r = 1.5'$  region centered on the AGN, we obtain for the AGN component a slope of  $-2.0^{+0.3}_{-0.4}$  and a column density of  $4.8^{+1.2}_{-1.1} \times 10^{23} \text{ cm}^{-2}$ , in agreement with the *Ginga* wide-angle fit (Ueno et al. 1994). The temperature of the surrounding cluster component is also in agreement with Ueno et al. Reynolds & Fabian (1996) detect a cooling flow around Cygnus A in the *ROSAT* data. A cooling flow component is not required in our fit, nor is it excluded, due to the spectral complexity of the AGN region. A radial profile, centered on the cluster large-scale centroid between the colliding subclusters, is shown in Fig. 4.

*Triangulum Australis*.—Temperature, pressure, and entropy maps of this hot cluster are discussed in MSI, who find an indication for nonadiabatic heating of the intracluster gas. Here we present the cluster's radial temperature profile. MSI noted a problem with the fit to the central  $r = 3'$  region of this cluster. A smaller,  $r = 1.5'$  central bin which we use here (in addition to including lower-energy *ASCA* data) requires an additional spectral component with 99% confidence. From *ASCA* data alone, we cannot distinguish between a power-law and a cooling flow component with a high upper temperature. *ROSAT* PSPC data which are sensitive to the presence of cool gas, do not require a cooling flow (MSI), therefore, a nonthermal contribution is more plausible. A complex spectrum in the central radial bin, denoted by the gray band in Fig. 4, does not significantly affect measurements in the outer annuli. The profile shows the temperature rising toward the cluster center.

##### 5. CORRECTING AVERAGE TEMPERATURES FOR COOLING FLOWS

We noted above that the presence of a strong cooling flow results in a significant underestimate of the cluster average temperature. The possibility of such underestimates was suggested earlier by Fabian et al. (1994b) as one explanation for the observed difference in the  $L_X - T$  relations for clusters with and without cooling flows. However, because spatially resolved

spectral data for clusters were unavailable, those authors did not foresee the amplitude of the underestimate that we observe. Since cooling flows (for a review see, e.g., Fabian 1994) occupy a small fraction of the cluster volume and are governed by different physics than the rest of cluster gas, their contribution should be excluded from the temperature estimates, if one intends to compare the global cluster properties with theoretical and numerical predictions that at present cannot model radiative cooling in detail.

The temperature maps and profiles presented above provide the necessary data to calculate average gas temperatures corrected for cooling flows and any unrelated sources that contaminated earlier, unresolved data. To do this, we integrate temperatures over all regions of a map or a profile with weights equal to the *ROSAT* flux in the respective region (which for the temperature range of our sample essentially means weighting with the emission measure). For the central bins, only the main thermal component (weighted by the total emission measure minus the best-fit cooling flow fraction) was used. Confidence intervals on weighted temperatures were calculated by Monte-Carlo simulations to take into account correlations between the temperature measurements in different regions. Using a map or a profile for this procedure did not result in significant differences in the weighted temperatures. The resulting weighted temperatures,  $T_X$ , are given in Table 1. The table shows that, as expected, the weighted temperatures are consistent with the single-temperature fits for clusters without cooling flows or other obvious spectral complications. Strong cooling flow clusters have significantly higher mean temperatures than their single-temperature fits imply, with the greatest difference, by a factor of 1.3, obtained for A1795. A separate paper (Markevitch et al. 1998b) shows that the difference between the  $L_X - T$  relations for clusters with and without cooling flows essentially disappears when these weighted temperatures and the luminosities with excised cooling flows are used. Such an improvement strongly suggests that our correction indeed results in more physically meaningful temperatures. We will use these temperatures below to normalize the radial temperature profiles and estimate cluster virial radii.

##### 6. THE COMPOSITE TEMPERATURE PROFILE

Figure 4 shows that, with a few exceptions, cluster temperatures significantly decline with radius. Those few clusters that do not show a general temperature decline are either ongoing mergers (e.g., A3667) or highly asymmetric clusters (e.g., A3395) for which radial profiles do not have much physical meaning. Below we show that temperature profiles of azimuthally symmetric clusters are similar when compared in physical units.

We normalize the radial temperature profile for each cluster by the weighted average temperature  $T_X$  obtained in §5, and plot it against the radius in units of  $r_{180}$ , within which the mean density (total mass divided by volume) is 180 times the critical density. This radius is approximately the radius of the virialized region for clusters (the virial radius) in an  $\Omega = 1$  universe (e.g., Lacey & Cole 1993). It is natural to scale radii by the virial radius, because cluster total density profiles are expected to be similar in these units (e.g., Bertschinger 1985). The scaled radii are independent of the Hubble constant.

We estimate  $r_{180}$  from our weighted temperatures using the Evrard, Metzler, & Navarro (1996, hereafter EMN) fit to the simulations,  $r_{180} = 1.95 h^{-1} \text{ Mpc} (T_X/10 \text{ keV})^{1/2}$ . Although the

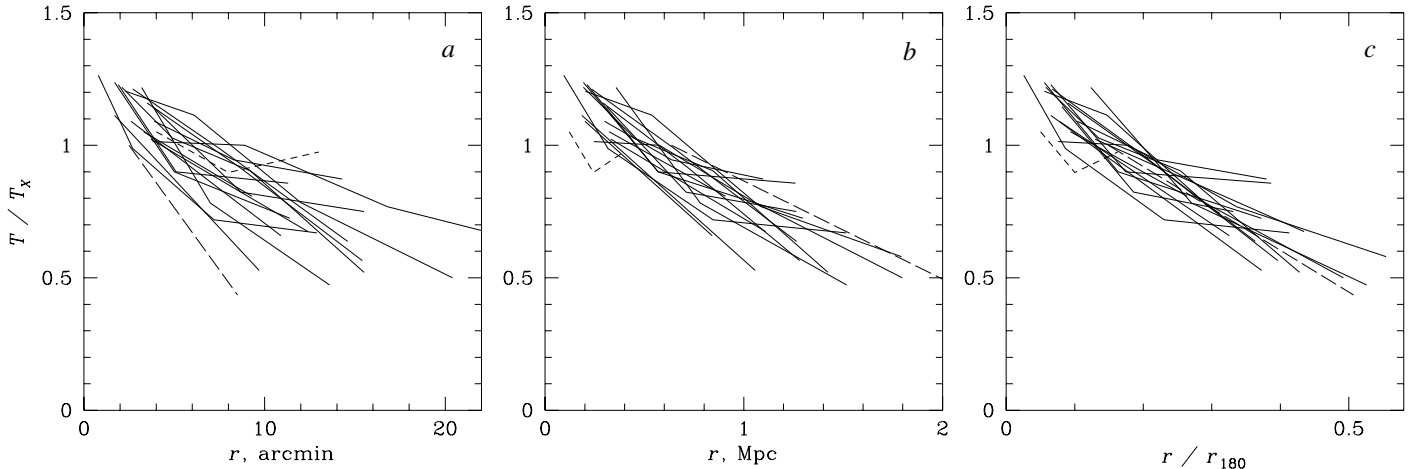


FIG. 5.—Normalized temperature profiles for relatively symmetric clusters, plotted against radii in (a) arcminutes, (b) megaparsecs, and (c) in units of  $r_{180}$ . Error bars are not shown for clarity. Shown for comparison are nearby AWM7 (short-dashed line) and distant A2163 (long-dashed line), which are not part of the sample. Cluster profiles are quite different in detector units (a), but are rather similar in physical units (b and c).

simulations generally do not reproduce the observed temperature profiles (see §7.2.3 below) and, therefore, this relation may be inaccurate, we are mostly interested in the scaling of  $r_{180}$  with  $T_X$  which is unlikely to be seriously wrong. We exclude from this exercise all 5 clusters with  $z > 0.08$  (A478, A1650, A1651, A2142, and A2597) because of large errors in their profiles, and 6 clusters with strongly asymmetric images (A119, A754, A3376, A3395, A3667, and Cygnus A) because their radial profiles have little meaning. Note that we do not specifically exclude mergers but only those of them with asymmetric images, due to the above consideration. For comparison, we include projected temperature profiles for two clusters that are not part of the sample due to their redshifts, A2163 at  $z = 0.201$  from M96, and AWM7 at  $z = 0.018$  from MV97a.

Figure 5 shows normalized temperature profiles (without error bars for clarity) plotted together against radius in arcminutes, megaparsecs, and in units of  $r_{180}$ . Central temperature values with large uncertainties are not shown. It is clear from the figure that in angular (detector) units, clusters have quite different temperature profiles. However, the profiles become rather similar in linear distance units and still more similar when plotted against radius in units of  $r_{180}$ . This comparison strongly suggests that we are observing a physical temperature decline rather than some unaccounted for instrumental effect.

In Fig. 6(a, b), we plot two subsets of the clusters shown in Fig. 5, the five coolest ( $T_X \leq 5.5$  keV) and hottest ( $T_X \geq 8$  keV) clusters. There is no apparent systematic difference between them. Note that if we were accounting for the ASCA PSF incorrectly, one would expect systematic differences between cooler and hotter clusters, because the effects of PSF scattering are greater at higher energies. Panels c, d, e in Fig. 6 show, respectively, temperature profiles for strong cooling flow clusters that are thought to be the most relaxed, strong mergers and asymmetric clusters (including those not shown in Fig. 5), and only the asymmetric clusters excluded from Fig. 5. There is no strong qualitative difference between the profiles in these subsets except for the large scatter for asymmetric clusters, and a possibly shallower median slope for the excluded clusters. The shallower slope is in part due to the fact that our profiles are not centered on the brightness peaks but centered on the large-scale

emission centroids between the subclusters. Normalized profiles of the five high-redshift clusters in our sample that we do not use because of large errors are consistent with the others.

We now try to quantify the slope of our composite radial temperature profile using a polytropic relation. Figure 7 shows profiles of symmetric clusters (those in Fig. 5 excluding AWM7 and A2163). Also plotted is an approximate band that encloses most profiles and their error bars. We assume a gas distribution with the core radius  $a_x = 0.15 h^{-1}$  Mpc and  $\beta = 0.67$  typical for our cluster sample median temperature of 7 keV (Jones & Forman 1997), and  $r_{180} = 1.63 h^{-1}$  Mpc which corresponds to this temperature. The observed temperature decline between 1 and  $6 a_x$  (0.09 and  $0.55 r_{180}$ ) in Fig. 7 corresponds to a polytropic index  $\gamma \simeq 1.24^{+0.20}_{-0.12}$ . The error on  $\gamma$  corresponds to the width of the 90% error band at large radii as shown in Fig. 7. A simple polytropic dependence is not a particularly good description of the composite profile; the ratio of temperatures between 1 and  $3 a_x$  corresponds to  $\gamma \simeq 1.19$  while the ratio between 3 and  $6 a_x$  corresponds to  $\gamma \simeq 1.29$ . For individual clusters, this equivalent polytropic index would of course depend on the individual gas density profile and the appropriate scaling of  $r_{180}$ , and in fact may be quite different from these values. We did not attempt to derive a more physically motivated functional form for the composite temperature profile. It should be searched for among the solutions of the hydrostatic equilibrium equation for various forms of the dark matter distribution; this issue will be addressed in a separate paper.

## 7. DISCUSSION

### 7.1. Merger Fraction

The last column in Table 1 marks those clusters in which our temperature maps (or entropy maps for A3395 and Triangulum Australis) indicate significant merging. Such clusters constitute about 1/3 of the sample. In addition, there are three clusters in the sample, A2142, A3266, and A3376, whose ROSAT images undoubtedly indicate mergers in progress but for which we were unable to probe temperature structure due to limited angular resolution or statistics. Even though for these clusters, a high resolution image appears to be a more sensitive indi-

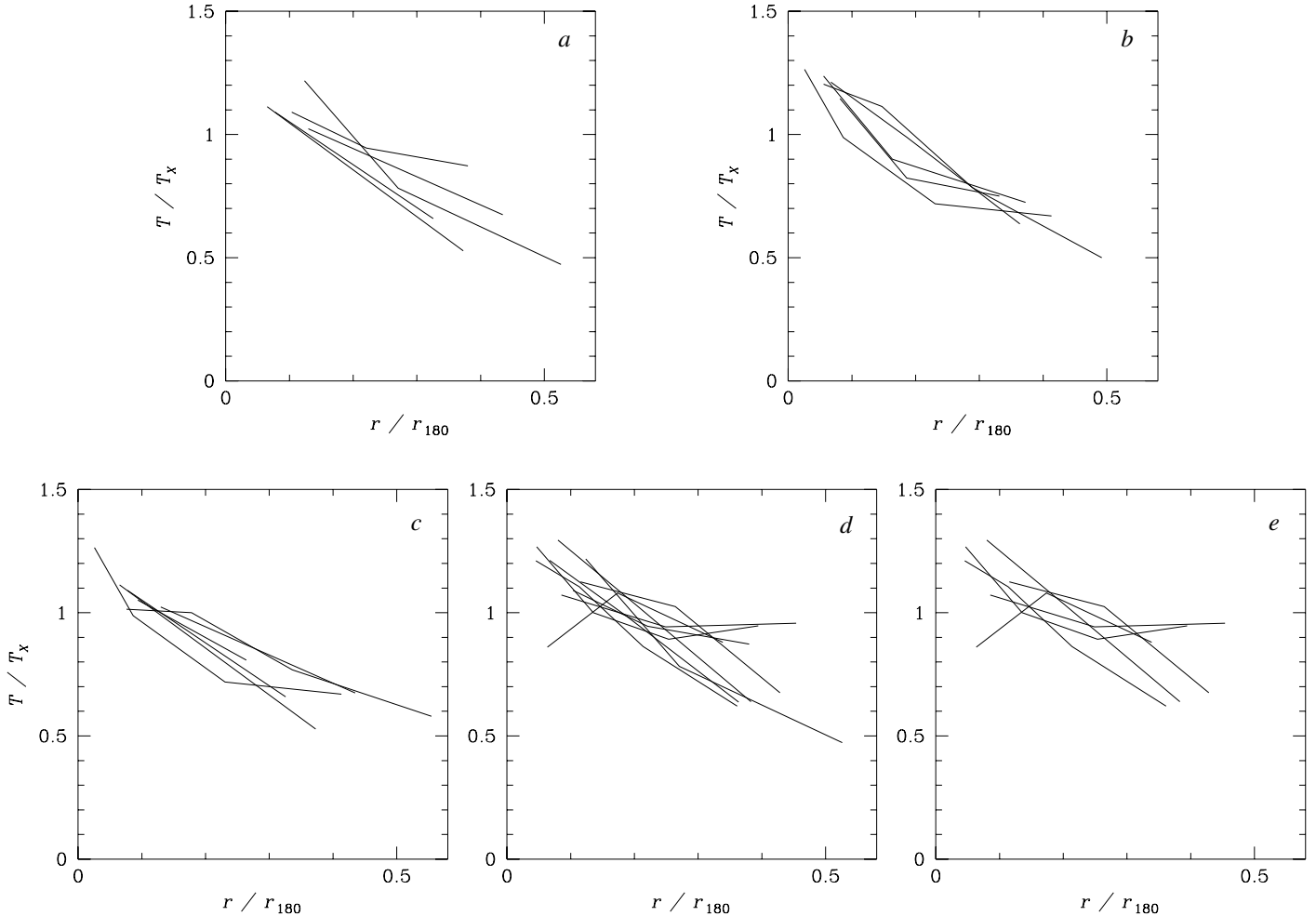


FIG. 6.—Normalized temperature profiles of several cluster subsets. Panels (a) and (b) show five coolest ( $T_x \leq 5.5$  keV) and five hottest ( $T_x \geq 8$  keV) clusters of those shown in Fig. 5 (excluding AWM7 and A2163), respectively. Panel (c) shows relaxed clusters with cooling flows (A780, A1795, A2029, A3112, A3571, A4059), panel (d) shows asymmetric and strong merger clusters (A119, A754, A2065, A3266, A3376, A3395, A3558, A3667, Cygnus A), and panel (e) shows only the asymmetric clusters excluded from Fig. 5 (A119, A754, A3376, A3395, A3667, Cygnus A). There is no apparent systematic difference between the subsamples, except for a greater scatter and slightly less steep decline of profiles for irregular clusters (panels d and e).

cator of merging, note that in general, image interpretation is often ambiguous and gas temperature maps can help to determine whether the structures in the image result from projection or from physical interaction. For example, as our temperature maps showed, the two A2256 subclusters (Briel et al. 1991) are probably separated along the line of sight (M96; MV97b), while the subcluster in A85 previously thought to be projected on the main cluster (e.g., Durret et al. 1997) is most likely merging. Among other examples of ambiguous images are two relatively symmetric subclusters in the Cygnus A cluster and the elliptical cluster A2065. For both of these, temperature maps indicate major mergers. Thus, in total, about half of the sample shows signs of ongoing mergers. Examination of *ROSAT* and *Einstein* images of those clusters that satisfy our selection criteria but are not included in the sample shows that they are not biased toward either mergers or relaxed systems. Therefore, our sample should be representative of the cluster merger fraction. The frequency of mergers is an indicator of the rate of cluster formation which depends on cosmology (e.g., Richstone, Loeb, & Turner 1992). Temperature maps of mergers provide infor-

mation complementary to that contained in the image, such as evidence for physical interaction, the merger direction, the collision velocity, etc. This makes them potentially more discriminating between cosmological models than tests based on the frequency of substructure in images alone (e.g., Tsai & Buote 1996; Thomas et al. 1997). A detailed comparison with cosmological simulations capable of modeling shocks would be necessary to obtain interesting constraints.

## 7.2. The Composite Temperature Profile

The main result of our paper is the observed similarity of cluster temperature profiles in units of average temperatures and virial radii. We discuss some implications of this finding below, after commenting on relevant earlier work.

### 7.2.1. Comparison with Earlier Work

Since *ASCA* is the first instrument offering the possibility of (almost) direct spatially resolved cluster temperature measurements, it is difficult to find accurate earlier data with which to

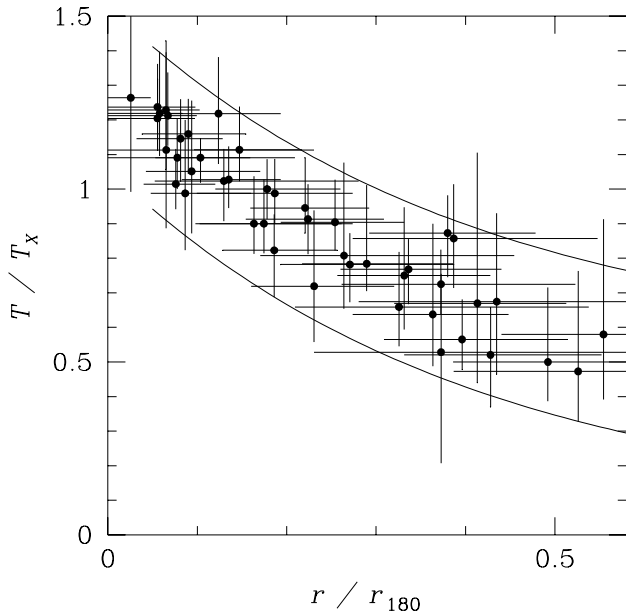


FIG. 7.—Normalized profiles of symmetric clusters (those shown in Fig. 5 without AWM7 and A2163) with their 90% errors. Smooth curves show an approximate band that encloses profiles and their errors.

compare our findings. Pre-*ASCA* spatially resolved temperature measurements were mostly limited to the nearby clusters Coma and Perseus. The Coma radial temperature profile obtained by Hughes et al. (1988) from *EXOSAT* is in rather good qualitative agreement with our composite profile. The *Spacelab-2* profile for Perseus (Eyles et al. 1991) only covers relatively small radii, but it agrees with our composite profile when the cooling flow is taken into account. Modeling data from *Einstein* SSS and *HEAO-1* that have different fields of view, Henriksen & White (1996) find that several cooling flow clusters, including A85 and A1795, have components outside the cooling flow regions that are hotter and cooler than the single-temperature fit. This is qualitatively similar to what we find in our direct measurements. MV97a obtained a temperature profile for A2256 using *ROSAT* PSPC which is in excellent agreement with the *ASCA* profile, although with large errors due to the limited PSPC energy band.

Other spatially-resolved *ASCA* temperature measurements are available; we discuss only those which properly include the effects of the PSF. The Ikebe et al. (1997) results for the Hydra A cluster are similar to our independent analysis. The *ASCA* analyses of the outer regions for nearby relatively regular clusters such as Perseus, Coma, and AWM7 are complicated by the presence of stray light; nevertheless, some preliminary results have appeared. Honda et al. (1996) have derived a temperature map for Coma which may indicate some radial temperature decline, although Coma appears to have a complex temperature structure. (T. Ohashi 1997 communicates that a more sophisticated reanalysis results in even greater temperature variations.) A nearly isothermal temperature profile obtained by Ezawa et al. (1997) for the symmetric cluster AWM7 apparently disagrees with our composite profile; however, when a central cooling flow is taken into account (MV97a), the temperature in the central region increases as in other cooling flow

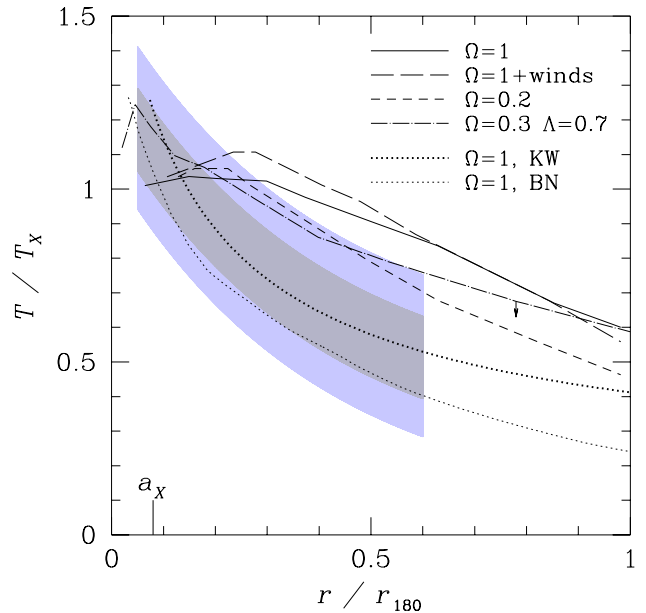


FIG. 8.—Temperature profiles from cluster simulations overlaid on our results. Light gray band is the same as that in Fig. 7; dark gray band encloses only the scatter of the best-fit values in Fig. 7. An approximate X-ray core radius for a 7 keV cluster is marked. Three-dimensional average profiles for  $\Omega = 1$ ,  $\Omega = 1+\text{winds}$ , and  $\Omega = 0.2$  models are from Evrard et al. (1996);  $\Omega = 0.3$ ,  $\Lambda = 0.7$  model is from Eke et al. (1997). Projection effect is shown by an arrow. Also shown are projected profiles from simulations of single clusters of Katz & White (1993) and Bryan & Norman (1997), both for  $\Omega = 1$ . The latter simulation is Eulerian, all others are Lagrangian.

clusters. The resulting AWM7 profile is consistent with the observed range of profiles. A definitive check of our results should be possible in the near future with *AXAF*.

### 7.2.2. Effect on Mass Estimates

The temperature profile is critical in deriving the gravitating mass under the assumption of hydrostatic equilibrium (e.g., Sarazin 1988). To evaluate the effect of the observed temperature decline on the mass estimates, we take a polytropic temperature profile with  $\gamma = 1.24$  which approximately represents our data for a typical 7 keV cluster (see §6). For the gas density parameters used in §6, the mass estimates within 1 and 6 core radii ( $0.15$  and  $0.9 h^{-1}$  Mpc) are approximately factors of 1.35 and 0.7 of the isothermal  $\beta$ -model estimates, respectively. This is similar to the results of a more detailed modeling of the A2256 *ASCA* data presented in MV97b (who find that the dark matter profile of the Navarro, Frenk, & White 1997 form was marginally allowed by the data but a steeper profile was preferred). It is also qualitatively similar to the A2029 *ASCA* analysis in Sarazin et al. (1997). As discussed in MV97b, the increased mass at small radii and decreased mass at large radii have several important implications, among them the convergence of the X-ray and lensing mass estimates at the cluster central regions and a steep rise of cluster baryon fraction with radius. The latter leads to a more pronounced “baryon catastrophe” (e.g., White et al. 1993) and probably indicates a presence of sources of gas thermal energy other than gravity and merger

shocks (e.g., David et al. 1995). A model-independent estimate of the average cluster total mass distribution using our composite temperature profile will be attempted in a later paper.

### 7.2.3. Comparison with Cluster Simulations

In Fig. 8, our composite temperature profile is shown by the light gray band which corresponds to the error band in Fig. 7, and by a less conservative dark gray band which approximates the scatter of the best-fit profile points. Overlaid on the data are radial temperature profiles from several published hydrodynamic cluster simulations with spatial resolution comparable to that of our measurements. We plot median temperature profiles for the simulated cluster samples from EMN (see also references therein), and the average profile from Eke, Navarro, & Frenk (1997; hereafter ENF). We also show profiles of single clusters whose growth was simulated by Katz & White (1993, hereafter KW; further details given in Tsai, Katz, & Bertschinger 1994) and Bryan & Norman (1997, hereafter BN). The smallest radii that we show represent the claimed spatial resolution in the simulations.

For the two steep KW and BN three-dimensional (i.e., not projected) temperature profiles, we performed the emission-weighted projection using the gas density distributions presented in the respective papers. Profiles from EMN and ENF are much shallower and the projection effect (illustrated approximately by an arrow in Fig. 8) is small; these profiles are shown without projection. The EMN models are appropriately normalized by the authors using the X-ray emission weighted temperature. ENF report that X-ray temperatures of their simulated clusters are on average equal to the virial temperatures which they use to normalize the profiles. To normalize the KW profile, we use an average X-ray temperature given in Tsai et al. For BN cluster, we calculated the average temperature using the temperature and density profiles.

EMN simulated clusters in  $\Omega = 1$  cosmological models with and without inclusion of galactic winds, and in an open model with  $\Omega = 0.2$ . They also present a flat model (cosmological constant  $\Lambda = 1 - \Omega$ ), which is in general agreement (except in the center) with the better-resolution ENF  $\Omega = 0.3$ ,  $\Lambda = 0.7$  simulation, and we show the latter. All these model profiles are in apparent disagreement with our results, being less steep than the observed profiles. The profile for the flat  $\Lambda$  model of ENF only marginally resembles our observations. The EMN  $\Omega = 0.2$  model and possibly the ( $\Omega = 1$  + winds) model may have the correct slope at  $r > 0.2r_{180}$ , but they, too, disagree within the overall range covered by the data. Note, however, that the central regions and the normalizations of the EMN profiles may be considerably incorrect, because their simulations did not resolve cluster cores where a large fraction of the X-ray emission originates. If their simulations underestimate temperatures in the cluster cores because of resolution effects (as is suggested by comparison of their and ENF results for flat  $\Lambda$  models), then an open model profile may succeed in describing the data.

The no-winds  $\Omega = 1$  model of EMN is in disagreement with the observations. However, an independent simulation assuming an  $\Omega = 1$  cosmology by KW, who employed the same Lagrangian approach with resolution comparable to EMN, but including radiative cooling, produced a very different temperature profile. The KW profile is in agreement with our observations. A high-resolution Eulerian simulation of an  $\Omega = 1$  cluster by BN (which did not include cooling) also produced a steeper temperature profile. KW and BN followed the evolution of only one

cluster in each case, and it is unclear to what extent their particular cluster realizations are representative. However, BN report that the dark matter profile of their cluster is well fit by the “universal” profile of Navarro et al. (1997) that fits most simulations with comparable resolution, suggesting that their cluster realization may be close to a typical cluster.

Because simulations do not reproduce the observed temperature profiles, the  $T_X - r_{180}$  relation from EMN that we used to scale the observed profiles may be incorrect. Indeed, the MV97b mass profile measured for A2256 corresponds to an  $r_{180}$  a factor of 1.15 smaller than predicted. This means that our temperature data may in fact subtend a larger fraction of  $r_{180}$  than shown in Fig. 8. This difference is small and will not qualitatively alter the comparison with models.

We excluded very asymmetric clusters (6 out of 21) in order to obtain a meaningful composite radial profile. In principle, this can bias our comparison with simulations that apparently do not make such a selection. However, as we noted in §6, the excluded cluster profiles are not qualitatively different and would only add scatter to the composite profile. A possibly shallower median slope of the 6 excluded clusters (Fig. 6e) is within the scatter of the profiles shown in Figs. 7 and 8 and therefore will not change any of our conclusions.

The comparison presented above shows that our temperature profile can potentially provide a useful constraint for cluster formation models and, possibly, for the underlying cosmology. At present, however, the disagreement among different simulation techniques is greater than the uncertainty of our measurements. It is also noteworthy that none of the simulations discussed above reproduces the observed shallow gas density profiles (see, e.g., Jones & Forman 1984 for a large sample; Briel, Henry, & Böhringer 1992 and Elbaz, Arnaud, & Böhringer 1995 for data at large cluster radii). A possible exception is the model with galactic winds (Metzler & Evrard 1997, presented in EMN) that predicts a shallow gas profile for cool but not for hot clusters. The temperature and density distributions are related through the hydrostatic equilibrium equation, and if one is not predicted correctly then the other would also be in error, for a given dark matter profile. Therefore, in the short term, our temperature profiles underscore the need to improve the cluster simulations.

### 7.3. A Note of Caution

Finally, we would like to emphasize that the temperature profiles presented here are not direct measurements but result from considerable corrections for the complex scattering of the ASCA mirrors. Therefore, for almost all clusters in our sample, the errors are dominated by the systematic component, mainly due to the uncertainties in the ASCA PSF and effective area. If our current understanding of the ASCA instruments is significantly flawed, the likely result would be that all our temperature profiles become systematically steeper or shallower. Therefore, even though the true individual temperature values should be within our confidence intervals that include conservative estimates for all current uncertainties, the individual profiles shown in Fig. 7 cannot be averaged in any sense, because their errors are not independent.

## 8. SUMMARY

We systematically analyzed ASCA data for 26 nearby bright clusters and found that none of them is isothermal, excluding

those few for which our accuracy is insufficient. The gas temperature varies with position within each cluster by a factor of 1.3–2 and sometimes stronger. For most clusters, we were able to reconstruct crude two-dimensional gas temperature maps. These maps (together with the images for three clusters without accurate maps) show that half of the clusters in our sample exhibit signs of ongoing merging.

For all clusters, we obtained radial temperature profiles. Almost all clusters show a temperature decrease with radius. We excluded the most asymmetric clusters for which a radial profile has no meaning, and compared the normalized temperature profiles for the remaining clusters. While the profiles are different in angular (or *ASCA* detector) units, when plotted in radial units normalized to the estimated virial radius for each cluster, they are remarkably similar. For a 7 keV cluster with a typical gas density profile, the observed temperature decline can be characterized by a polytropic index of 1.2–1.3, although this is not a particularly good description over the range of measured radii.

The observed temperature decline implies that, at small radii, an analysis that assumes the hydrostatic equilibrium and a constant temperature underestimates the cluster mass, while at large radii, the gravitating mass falls below the isothermal estimate. In particular, for a 7 keV cluster with our median temperature profile and a typical gas density distribution, the total mass estimates within 0.15 and  $0.9 h^{-1}$  Mpc are approximately factors of 1.35 and 0.7 above and below the isothermal  $\beta$ -model estimates, respectively. As discussed in the study of A2256

(MV97b), this general result strengthens the argument for a low- $\Omega$  cosmology based on the high baryon fraction in clusters (e.g., White et al. 1993). It also implies a strong segregation of gas and dark matter, possibly indicating that sources other than gravity have produced a significant fraction of the gas thermal energy (e.g., David et al. 1995).

Finally, we compared our composite temperature profile to the results of cluster hydrodynamic simulations. We find that most simulations predict a considerably shallower average temperature decline, with the possible exception of those for low- $\Omega$  cosmologies. This comparison suggests that, potentially, the *ASCA* temperature profiles can constrain cluster formation models. However, at present, there is a discrepancy between different simulations that is greater than the uncertainty in our measurements. This underscores the need for further theoretical and numerical work before conclusions can be drawn regarding which cosmological parameters best describe the observations.

We thank all the members of the *ASCA* team for their work on acquiring the data analyzed here, and NASA/GSFC for maintaining the HEASARC online data archive which we used extensively. We are grateful to Ue-Li Pen and Nancy Brickhouse for useful comments. M. M. and W. R. F. acknowledge support from Smithsonian Institution, NASA grant NAG5-2611, and NASA contract NAS8-39073. C. L. S. was supported in part by NASA grants NAG5-2526 and NAG5-4516. A. V. was supported by CfA postdoctoral fellowship.

#### REFERENCES

- Abell, G. O., Corwin, H. G., Olowin, R. P. 1989, *ApJS*, 70, 1  
 Bahcall, J. N., & Sarazin, C. L. 1977, *ApJ*, 213, L99  
 Bertschinger, E. 1985, *ApJS*, 58, 39  
 Briel, U. G., et al. 1991, *A&A*, 246, L10  
 Briel, U. G., Henry, J. P., & Böhringer, H. 1992, *A&A*, 259, L31  
 Briel, U. G., & Henry, J. P. 1994, *Nature*, 372, 439  
 Briel, U. G., & Henry, J. P. 1996, *ApJ*, 472, 131  
 Bryan, G. L., & Norman, M. L. 1997, in *Computational Astrophysics, Proc. 12th Kingston Conference*, eds. D. Clarke & M. West (PASP), astro-ph/9710186 (BN)  
 Buote, D. A., & Tsai, J. C. 1996, *ApJ*, 458, 27  
 David, L., Jones, C., & Forman, W. 1995, *ApJ*, 445, 578  
 David, L., Slyz, A., Jones, C., Forman, W., Vrtilik, S. D., & Arnaud, K. A. 1993, *ApJ*, 412, 479  
 Dickey, J. M., & Lockman, F. J. 1990, *ARA&A*, 28, 215  
 Donnelly, R. H., Markevitch, M., Forman, W., Jones, C., Churazov, E., Gilfanov, M., & David, L. P. 1997, *ApJ*, submitted  
 Dotani, T., Yamashita, A., Rasmussen, A., & the SIS team, 1995, *ASCA Newsletter*, # 3 (NASA/GSFC)  
 Durret, F., Forman, W., Gerbal, D., Jones, C., & Vikhlinin, A. 1997, *A&A*, to be submitted  
 Ebeling, H., Voges, W., Böhringer, H., Edge, A. C., Huchra, J. P., & Briel, U. G. 1996, *MNRAS*, 281, 799  
 Edge, A. C., & Stewart, G. C. 1991, *MNRAS*, 252, 414  
 Edge, A. C., & Stewart, G. C., & Fabian, A. C. 1992, *MNRAS*, 258, 177  
 Eke, V. R., Navarro, J. F., & Frenk, C. S. 1997, *ApJ*, submitted; astro-ph/9708070 (ENF)  
 Ettori, S., Fabian, A. C., & White, D. A. 1997, *MNRAS*, in press  
 Evrard, A. E., Metzler, C. A., & Navarro, J. F. 1996, *ApJ*, 469, 494 (EMN)  
 Eyles, C. J., Watt, M. P., Bertram, D., Church, M. J., & Ponman, T. J. 1991, *ApJ*, 376, 23  
 Ezawa, H., Fukazawa, Y., Makishima, K., Ohashi, T., Takahara, F., Xu, H., & Yamasaki, N. 1997, *ApJ*, 490, L33  
 Fabian, A. C. 1994, *ARA&A*, 32, 227  
 Fabian, A. C., Arnaud, K. A., Bautz, M. W., & Tawara, Y. 1994a, *ApJ*, 436, L63  
 Fabian, A. C., Crawford, C. S., Edge, A. C., & Mushotzky, R. F. 1994b, *MNRAS*, 267, 779  
 Fabian, A. C., Peres, C. B., & White, D. A. 1997, *MNRAS*, 285, L35  
 Frenk, C. S., et al. 1998, in preparation  
 Fujita, Y., Koyama, K., Tsuru, T., & Matsumoto, H. 1996, *PASJ*, 48, 191  
 Gendreau, K., & Yaqoob, T. 1997, *ASCA Newsletter*, # 5 (NASA/GSFC)  
 Gotthelf, E. 1996, *ASCA Newsletter*, # 4 (NASA/GSFC)  
 Hatsukade, I. 1989, Ph.D. thesis, Osaka Univ.  
 Henriksen, M., & Markevitch, M. 1996, *ApJ*, 466, L79  
 Henriksen, M. J., & White, R. E. 1996, *ApJ*, 465, 515  
 Henry, J. P., & Briel, U. G. 1995, *ApJ*, 443, L9  
 Henry, J. P., & Briel, U. G. 1996, *ApJ*, 472, 137  
 Honda, H., et al. 1996, *ApJ*, 473, L71  
 Huang, Z., & Sarazin, C. L. 1998, *ApJ*, 496, in press  
 Hughes, J. P., Gorenstein, P., & Fabricant, D. 1988, *ApJ*, 329, 82  
 Ikebe, Y., et al. 1996, *Nature*, 379, 427  
 Ikebe, Y., et al. 1997, *ApJ*, 481, 660  
 Ishisaki, Y., 1996, PhD thesis, University of Tokyo  
 Jones, C., Donnelly, H., Forman, W., Markevitch, M., Vikhlinin, A., Churazov, E., & Gilfanov, M. 1997, in *Untangling Coma Berenices*, Marseilles, ed. A. Mazure (World Scientific), in press  
 Jones, C., & Forman, W. 1984, *ApJ*, 276, 38  
 Jones, C., & Forman, W. 1997, *ApJS*, submitted  
 Katz, N., & White, S. D. M. 1993, *ApJ*, 412, 455 (KW)  
 Kellogg, E. M., Gursky, H., Tananbaum, H., Giacconi, R., & Pounds, K. 1972, 174, L65  
 Koyama, K., Takano, S., & Tawara, Y. 1991, *Nature*, 350, 135  
 Lacey, C., & Cole, S. 1993, *MNRAS*, 262, 627  
 Loewenstein, M. 1997, in *X-ray Imaging and Spectroscopy of Cosmic Plasmas*, ed. F. Makino (Tokyo: Universal Academy), 67  
 Makishima, K. 1996, *ASCA calibration memo*  
 Markevitch, M. 1996, *ApJ*, 465, L1 (M96)  
 Markevitch, M., et al. 1998a, in preparation (M98)  
 Markevitch, M., et al. 1998b, in preparation  
 Markevitch, M., Mushotzky, R. F., Inoue, H., Yamashita, K., Furuzawa, A., & Tawara, Y. 1996a, *ApJ*, 456, 437  
 Markevitch, M., Sarazin, C. L., & Irwin, J. A. 1996b, *ApJ*, 472, L17 (MSI)  
 Markevitch, M., & Vikhlinin, A. 1997a, *ApJ*, 474, 84 (MV97a)  
 Markevitch, M., & Vikhlinin, A. 1997b, *ApJ*, in press (MV97b)  
 Markevitch, M., Yamashita, K., Furuzawa, A., & Tawara, Y. 1994, *ApJ*, 436, L71  
 Mathews, W. G. 1978, *ApJ*, 219, 413  
 Metzler, C. A., & Evrard, A. E. 1997, *ApJ*, submitted (astro-ph/9710324)  
 Mitchell, R., Culhane, J., Davison, P., & Ives, J. 1976, *MNRAS*, 189, 329  
 Navarro, J. F., Frenk, C. S., & White, S. D. M. 1997, *ApJ*, in press  
 Owen, F. N., Ledlow, M. J., Morrison, G. E., & Hill, J. M. 1997, *ApJ Letters*, in press (astro-ph/9708150)  
 Ponman, T. J., & Bertram, D. 1993, *Nature*, 363, 51  
 Press, W. H., Teukolsky, S. A., Vetterling, W. T., & Flannery, B. P. 1992, *Numerical Recipes* (Cambridge University Press)  
 Reynolds, C. S., & Fabian, A. C. 1996, *MNRAS*, 278, 479  
 Richstone, D., Loeb, A., & Turner, E. L. 1992, *ApJ*, 393, 477

- Roettiger, K., Burns, J., & Loken, C. 1993, *ApJ*, 407, L53
- Sarazin, C. L. 1988, *X-ray Emission from Clusters of Galaxies* (Cambridge: Cambridge University Press)
- Sarazin, C. L., & Graney, C. M. 1991, *ApJ*, 375, 532
- Sarazin, C. L., & McNamara, B. R. 1997, *ApJ*, 480, 203
- Sarazin, C. L., Wise, M. W., & Markevitch, M. L. 1997, *ApJ*, submitted
- Schindler, S., & Müller, E. 1993, *A&A*, 272, 137
- Serlemitsos, P. J., et al. 1995, *PASJ*, 47, 105
- Snowden, S. L., McCammon, D., Burrows, D. N., & Mendenhall, J. A. 1994, *ApJ*, 424, 714
- Soltan A. J., Hasinger, G., Egger, R., Snowden, S., & Trümper, J. 1996, *A&A*, 305, 17
- Takahashi, T., Markevitch, M., Fukazawa, Y., Ikebe, Y., Ishisaki, Y., Kikuchi, K., Makishima, K., & Tawara, Y. 1995, *ASCA Newsletter*, # 3 (NASA/GSFC)
- Tanaka, Y., Inoue, H., & Holt, S. S. 1994, *PASJ*, 46, L37
- Thomas, P. A., et al. 1997, *MNRAS*, submitted (astro-ph/9707018)
- Tsai, J. C., & Buote, D. A. 1996, *MNRAS*, 282, 77
- Tsai, J. C., Katz, N., & Bertschinger, E. 1994, *ApJ*, 423, 553
- Ueno, S. 1996, PhD thesis, University of Tokyo
- Ueno, S., Koyama, K., Nishida, M., Yamauchi, S., & Ward, M. J. 1994, *ApJ*, 431, L1
- Vikhlinin, A., & Forman, W. 1995, *ApJ*, 455, L109
- Watt, M. P., Ponman, T. J., Bertram, D., Eyles, C. J., Skinner, G. K., & Willmore, A. P. 1992, *MNRAS*, 258, 738
- Way, M. J., Quintana, H., & Infante, L. 1997, *ApJ*, submitted (astro-ph/9709036)
- White, D. A., Fabian, A. C., Allen, S. W., Edge, A. C., Crawford, C. S., Johnstone, R. M., Stewart, G. C., & Voges, W. 1994, *MNRAS*, 269, 589
- White, S. D. M., Navarro, J. F., Evrard, A. E., & Frenk, C. S. 1993, *Nature*, 366, 429
- White, S. D. M., & Rees, M. J. 1978, *MNRAS*, 183, 341